

MASTER IN PHYSICS OF COMPLEX SYSTEMS

**Theory and application of
multifractal analysis methods in
images for the study of soil
structure**

Author

Iván González Torre

Tutors

Ana María Tarquis Alfonso

Juan Carlos Losada González

Acknowledgements

First I would like to express mi gratitude to my master thesis work tutors: Ana María Tarquis and Juan Carlos Losada, for their continuous support, motivation, advises and knowledge. Their guidance helped me in all time the time of research and writing of this work.

I also want to thank specially to Bartolome Luque and to all of the personal of Numerical Methods in Aerospace Technology department for their support and friendship every day.

My sincere thanks also goes to all Complex System Department Group for offering me my first opportunity in the researching world some years ago.

I am grateful to Richard Heck from Gelp University and to the Research Centre for the Management of Agricultural and Environmental Risks (CEIGRAM) for giving me the economical support doing this study.

Last but not the least I would like to thank to my family: my parents Pedro and M Carmen always supporting my studies and projects and to my sister Edurne for always being a good reference in the life.

Abstract

This work focuses to study soil structure as a complex system characterizing it through their multiscaling behaviour. The soil performs important functions as a medium for plant growth, water storage, modifier of the atmosphere and it is a habitat for organisms. Soil structure can be modelled as the spatial arrangement of soil particles, aggregates and pores. Fractal geometry has been increasingly applied to quantify soil structure, using fractal generalized dimensions for explaining the complexity of its structure.

Thanks to the X-ray Computed Tomography (CT-Scan) soil samples can be analysed in high resolution. CT-Scan is a relatively recent non-destructive testing method which offers an attractive opportunity for the three-dimensional insight of the inner structure of objects and materials. The ultimate product of the tomography process is the slice, which represents a virtual thin-section of the sample, whose thickness is strictly related to the achievable X-ray computed tomography spatial resolution. A grayscale value is assigned to each voxel of the reconstructed slice, proportionally to the local X-ray attenuation map. Once a set of consecutive slices is reconstructed, it is possible to create a three-dimensional digital data set of the sample just combining the slices into a stack.

For studying the image stacks we have developed a JAVA plug-in for the image analysis software, ImageJ. After a review of the multifractal theory we have selected the gliding and box counting methods for multifractal and monofractal analysis and implemented in the program. We have satisfactorily tested it with the theoretical and real data, and full documented writing a User manual.

Then we have studied several planes in the main directions of a soil aggregate comparing them. Although the study has shown interesting results, the main conclusion is that two-dimensional analysis is not enough for explaining the overall complexity of the structure. Finally, three soil samples ploughed with different tillage tools has been characterized with the multifractal methods applying a full three-dimensional analysis. Comparison of computing times and the goodness of the results are showed.

Contents

1	Introduction	1
2	Soil's relevance	3
3	Fractals and multifractals methods	7
3.1	Box Counting method	8
3.1.1	Monofractal analysis	8
3.1.2	Multifractal analysis	8
3.2	Gliding method	9
4	Materials and methods	11
4.1	CT-scan	11
4.2	Software development	12
5	Results	15
5.1	Soil aggregates sample	15
5.1.1	Two-dimensional analysis	16
5.1.2	Three-dimensional analysis	24
5.2	Tillage treatments	27
5.2.1	Moldboard	29
5.2.2	Chissel	32
5.2.3	Roller	35
5.2.4	Multifractal comparison	38
6	Conclusions	41

Bibliography	43
Appendices	45
A $X(q, \epsilon)$ list of 2D slices of soil aggregates sample calculated with different methods	47
B $X(q, \epsilon)$ list of 3D soil aggregates sample analysed with different methods and sizes	57
C $X(q, \epsilon)$ list of 3D tillage treatments soil samples analysed	61
D User manual and documentation of the plug-in implemented in ImageJ for multifractal analysis	67

Chapter 1

Introduction

In this dissertation we pretend to understand the complexity of the soil's structure characterizing them through multiscale analysis. For this purpose we have made a complete review about the multifractal methods for applying to two-dimensional and three-dimensional images of soils. The most suitable methods for this task has been selected.

In Chapter 2 is explained the relevance of the soil for the ecosystem and human life as well as its composition and structure. In Chapter 3 there is a review of fractal and multifractal methods employed along this research.

For analysing the images we have developed a software written in JAVA which is able to analyse 2D and 3D in black and white or gray images. The material and methods employed are explained in Chapter 4 while the user manual and documentation of the software can be found in Appendix D. The software has been validated with real and published data getting excellent results.

In Chapter 5 we have analysed some real soil samples in 2D and 3D, comparing them and obtained significant conclusions summarized in Chapter 6

Chapter 2

Soil's relevance

Soil is a major component of the Earth's ecosystem. From ozone depletion and global warming to rain forest destruction and water pollution, the world's ecosystems are impacted in far-reaching ways by the processes out in the soil. Soil is the largest superficial carbon and global carbon reservoir on Earth, and it is potentially one of the most reactive to human disturbance and climate change. As the planet warms, soils will add additional dioxide into the atmosphere due to its biological activity increment. Thus, soil carbon losses likely have a huge feedback response to global warming. [1]

Soil acts as an engineering medium, a habitat for soil organisms, a recycling system for nutrients and organic wastes, a regulator of water quality, a modifier of atmospheric composition, and a medium for plant growth. Since soil has a tremendous range of available niches and habitats, it contains most of the earth's genetic diversity. A handful of soil can contain billions of organisms, belonging to thousands of species. [2]

The soil performs very important functions: it is a medium for plant growth, it is a water storage, it is a modifier of the atmosphere and it is an habitat for organism. In the soil we grove the plants we eat and the plants we feed the animals we eat. We walk and we build our homes there. Without a proper soil the life we know, would not be the same.

To understand and manage the natural systems it is necessary to study soil physical properties. The range of scale of the study is very wide: from microbial habitats to regional weather modelling. The soil data usually are obtained from

small soil samples and cores, yet the goal is to reconstruct soil physical properties across the fields.

Soil is a mixture of minerals, organic matter, gases, liquids and organism that can support plan life, see Figure 2.1. Soils supply plants with mineral nutrients held in place by the clay and humus content of the soil. For optimum plant growth, the generalized content of soil components by volume should be roughly 50% solids (45% mineral and 5% organic matter), and 50% voids of which half is occupied by water and half by gas. The percent soil mineral and organic content is typically treated as a constant, while the percent soil water and gas content is considered highly variable whereby a rise in one is simultaneously balanced by a reduction in the other.

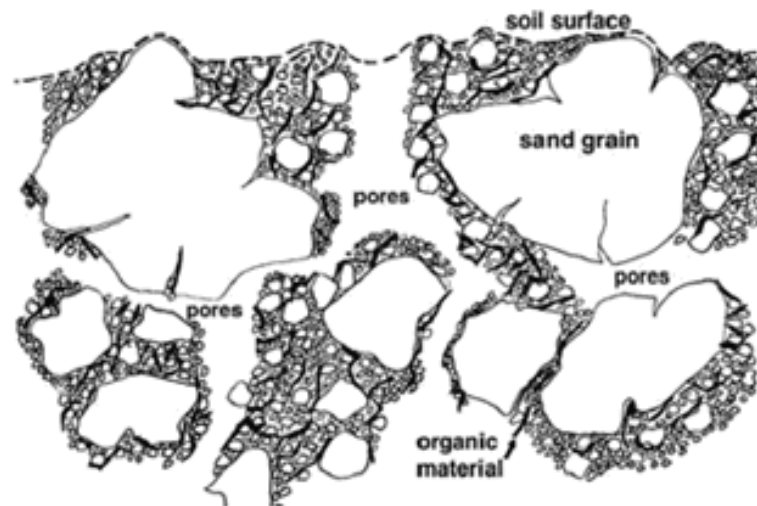


Figure 2.1: The illustration shows a typical distribution of solids and pores inside a soil sample

Soil structure can be modelled as the spatial arrangement of soil particles, aggregates and pores. The geometry of each one of these elements, as well as their spatial arrangement, has a great influence on the transport of fluids and solutes through there [3].The pore space allows for the infiltration and movement of air and water, both of which are critical for life in soil. Compaction, a common problem with soils, reduces this space, preventing air and water from reaching the

plant roots and soil organisms.

Fractal geometry has been increasingly applied to quantify soil structure, using fractal generalized dimensions for explaining the complexity of the structure. Scaling effects have been observed for a long time in soil physics, for example, soil bulk density with the sample size, specific surface areas varying as a function of observation scale, or an increasing number of small voids revealed with increased resolution. Fractal theory suggests that these scaling phenomena may be more the rule than the exception and can be explained by an underlying multiscale structure. The value of fractal parameters can be obtained directly through image analysis of a soil sample. [4]

One of the most direct methods of characterizing soil structure is the analysis of the spatial arrangement of pore and solid spaces on images of sections of resin-impregnated soil. Recent technological advances in digital imagery and computers have greatly facilitated the application of image analysis techniques in soil science. Thick sections are analysed by reflected light, and thin sections are analysed by transmitted light to obtain images from which pores and solid spaces can be separated using image analyses techniques. Direct measurements on images together with applications of set theory are used to quantify connectivity, size and shape of pores. However, the image resolution and the threshold value used to discriminate between pore and solid space can introduce errors in the method.

Scaling of pore systems could be characterized with fractal and multifractal techniques. The fractal approach assumes a hierarchical distribution of mass in space such that at any resolution the fractal structure is seen as the union of subjects similar to the whole. In this instance a single fractal dimension server to characterize the mass distribution.

Chapter 3

Fractals and multifractals methods

In this section it is introduced the methods used for calculating fractal and multifractal measures. From the most simple box counting fractal method to multifractal gliding method.

An object has its topological measure which is one of the several ways of defining the dimension of the space. For example, the topological dimension of a line is one, the dimension of surface is two, and the dimension of a 3D object is 3. However there are some natural and mathematical objects that exceeds their topological dimension. A geometrical fractal is a mathematical object which can exceeds its topological dimension and typically displays self-similar patterns, e.g., the borders of a country [5], the Koch snowflake [6] or Sierpinski triangle.

But often, the fractal measure is not enough for explaining the complexity in the different scales of an object, so the multifractal analysis is needed. Multifractals could be seen as an extension of fractals. Multifractal analysis initially appeared with multiplicatives cascades models of Mandelbrot for the study of energy dissipation in the context of the fully developed turbulence [7]. After that it has been implemented for several different natural systems.

There are several methods for compute the fractal dimension of an image, each one has its own theoretic basis. Here, we are going to use two of them: Box Counting and Gliding, which is an improved (but more computationally demanding) method for the low density areas of the image.

3.1 Box Counting method

This methodology defined by [8] is a classical in this field. It breaks the spatially extended dataset into smaller and smaller pieces (boxes) and analyse them at each smaller scale. One method of understanding this method is as zooming in observing how details change with scale. In the algorithm implemented the boxes are scaled in power of two sizes on. Therefore it is necessary processing the image that its size in pixels is a power of 2. So if the image is not in a properly size, it will be cut or resized.

3.1.1 Monofractal analysis

Let a $L \times L$ grid of $\epsilon \times \epsilon$ boxes, $N(\epsilon)$ be the number of boxes required to cover the black area in the image for each size. The fractal dimension of an image can be defined as the relationship between the number of non-empty boxes and the its size with the next expression [6]:

$$D = \lim_{\epsilon \rightarrow 0} \frac{\log N(\epsilon)}{\log \frac{1}{\epsilon}} \quad (3.1)$$

so the fractal dimension D , can be estimated numerically as the slope of the line:

$$\log N = D \log \frac{1}{\epsilon} + cte \quad (3.2)$$

3.1.2 Multifractal analysis

In the multifractal method, a distorting factor is applied to datasets extracted from the image for giving more or less importance to the high or low mass density areas of the picture.

Meshing the picture with boxes of size ϵ and define $P_i(\epsilon)$ as the probability of this mass at i relative to the total mass of the picture for a box size ϵ , then the generalized dimensions D_q which corresponds to scaling exponents for the q_{th} moments of the measure are defined as [9]:

$$D_q = \frac{1}{q-1} \lim_{\epsilon \rightarrow 0} \frac{\log \sum_i P_i^q(\epsilon)}{\log \epsilon} = \frac{1}{q-1} \lim_{\epsilon \rightarrow 0} \frac{\log X(q, \epsilon)}{\log \epsilon} \quad (3.3)$$

for $q \neq 1$ and being $X(q, \epsilon)$ the partition function. For $q = 1$, D_1 is defined by taking the limit when q approaches 1 and by using L'Hopital's Rule [10]:

$$D_1 = \lim_{\epsilon \rightarrow 0} \frac{\sum_i P_i(\epsilon) \log P_i(\epsilon)}{\log \epsilon} \quad (3.4)$$

This measure D_q is related with the mass exponent $\tau(q)$ as follows:

$$\tau_q = (q - 1)D_q \quad (3.5)$$

for $q \neq 1$ and in the case of conservative measure $\tau_1 = 0$.

Another interesting measure in multifractal analysis is the relationship between a Hausdorff dimension f and an average singularity strength α as implicit functions of the parameter q . Those are defined as follows:

$$f(\alpha) = q\alpha - \tau \quad (3.6)$$

$$\alpha = \frac{d\tau}{dq} \quad (3.7)$$

An easily used definition of the singularity spectrum which is the one that have been implemented in this ImageJ plug-in is: [11]

$$f(q) = \lim_{\epsilon \rightarrow 0} \frac{\sum_i \mu_i(q, \epsilon) \log \mu_i(q, \epsilon)}{\log \epsilon} \quad (3.8)$$

$$\alpha(q) = \lim_{\epsilon \rightarrow 0} \frac{\sum_i \mu_i(q, \epsilon) \log P_i(q, \epsilon)}{\log \epsilon} \quad (3.9)$$

where $\mu_i(q, \epsilon)$ is how the distorted mass probability at a box compares to the distorted sum over all boxes at this box size:

$$\mu_i(q, \epsilon) = \frac{(P_j(\epsilon))^q}{\sum_j (P_j(\epsilon))^q} \quad (3.10)$$

3.2 Gliding method

The problem of the Box Counting method is that for negative q values the errors are high. Gliding method has been developed for improving this handicap.

The gliding box method was originally used in lacunarity analysis and later modified by Cheng in [12] for application to multifractal analysis and then used in soil analysis [13]. This method constructs samples by gliding a box of certain dimensionless size ϵ over the grid map in all possible directions. An up-scaling partitioning process begins with a minimum line size smaller than 1. This method first estimates the mass exponent function $\tau(q)$:

$$\tau(q) + D = \lim_{\epsilon \rightarrow 0} \frac{\log\left(\frac{1}{N^*(\epsilon)} \sum_{i=1}^{N^*(\epsilon)} \mu_i^q(\epsilon)\right)}{\log \epsilon} \quad (3.11)$$

where ϵ is the dimensionless box size, $N^*(\epsilon)$ represents total number of gliding boxes of size ϵ with measure $\mu(\epsilon) \neq 0$ and D is the topological dimension of the object analysed ($D = 2$ for two-dimensional objects and $D = 3$ for three-dimensional objects)

The functions α and $f(\alpha)$ are estimated numerically by the Legendre transformation as

$$\alpha(q) = \frac{d\tau(q)}{dq}, \quad f(\alpha) = \alpha(q)q - \tau(q) \quad (3.12)$$

Here we suppose that the uncertainties of α are:

$$\Delta\alpha = \frac{\Delta\tau}{|\tau|} \alpha \quad (3.13)$$

The advantage of gliding box method is that the larger sample size it provides better statistical results. The disadvantage is that it is more computation demand because of the great number of operations.

Chapter 4

Materials and methods

4.1 CT-scan

The soil samples have been analysed with high-resolution X-ray Computed Tomography (CT-Scan). CT-Scan is a relatively recent non-destructive testing method which offers an attractive opportunity for the three-dimensional insight of the inner structure of objects and materials. Nowadays, due to the great technological advances and the computational power of modern calculators, CT systems are massively employed for a wide range of purposes in the scientific and industrial sectors, e.g. flaw detection, failure analysis, metrology and reverse engineering.

The basic components forming a CT system are the X-ray source, characterised by a micrometric or sub-micrometric focal spot size, the detection system, to collect the transmitted radiation emerging from the sample, and the sample positioning stages. The CT-Scan is done recording on the detector, which is placed behind the sample, a set of planar projections while the sample rotates inside the incident beam over approximately the angular range between 0 and 180/360 degrees. A sufficient number of those angular views should be acquired at regular or known steps, in order to efficiently reconstruct a set of horizontal cross sections (the slices) of the object by mean of a well-established mathematical procedure known as the filtered back-projection (FBP) algorithm. Its worth mentioning that the rotation of the sample is a relative movement: in medical-like scanner the patient is stationary and the source-detector block rotates, while in tabletop facilities typically the sample is moved. Figure 4.1 illustrates the main components needed

for CT-Scan. [14]

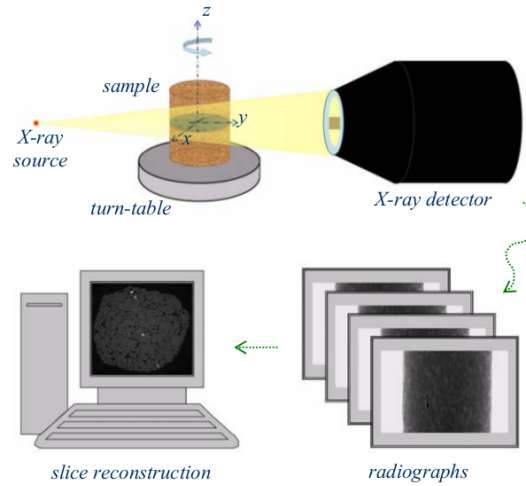


Figure 4.1: Main components of CT-Scan [14]

The ultimate product of the tomography process is the slice, which represents a virtual thin-section of the sample, whose thickness is strictly related to the achievable X-ray computed tomography spatial resolution. A grayscale value is assigned to each voxel 1 of the reconstructed slice, proportionally to the local X-ray attenuation map. Once a set of consecutive slices is reconstructed, it is possible to create a three-dimensional digital data set of the sample just combining the slices into a stack. [14]

4.2 Software development

Analyse the structure of 2D and 3D image samples is not a trivial task. For this purpose there are different methods and techniques. We have developed a specific software based in ImageJ plug-in. ImageJ is a public domain Java software specialized and optimized in image processing. It works with modules called plug ins.

ImageJ
Image Processing and Analysis in Java



Figure 4.2: ImageJ is a software specialized in image computing

We have developed 6 independent modules for multifractal analyse of images: 2D Box Counting Monofractal method, 2D Box Counting Multifractal method, 2D Gliding method, 3D Box Counting Monofractal method, 3D Box Counting Multifractal method and 3D Gliding method. All those plugins let the user choose between different options e.g. the min and max size of the boxes for the method and the values of q in multifractal method. It calculates the most important measures with their errors in multifractal analysis: $X(q, \epsilon)$, $\tau(q)$, fractal and multifractal generalized dimension Dq and multifractal spectrum α and $f(\alpha)$

The software has been tested successfully with theoretical, real and published data. We have also written a detailed user manual of the program which can be found as the Appendix D on this document. In that Appendix, there are instructions about its operation and some examples with their results.

Chapter 5

Results

For this task we have analysed 4 real soil samples. One of them is from a soil aggregates sample from a field of Scotland, while the other three have been extracted from the same experimental farm in Cordoba (Spain) but plowed with different tillage tools.

5.1 Soil aggregates sample

For this analysis, an arable sandy loam soil from a field of Scotland was packed into polypropylene cylinders of 6 cm diameter and 5 cm high at 1.2 Mgm-3 bulk density being air-filled pore volume 0.17. The soil samples were imaged using an mSIMCT at 155keV and 25 mA. To minimize beam hardening an aluminium filter (0.25 mm) was applied, and reconstruction process also implied several corrections. The image stacks of 260x260x256 with voxel-thick slices were generated from the 3D volumes by using VGStudioMax v.1.2.1.

We have reconstructed the 3 Dimensional model joining the slices with ImageJ. The 3D image can be seen in Figure 5.1 where the darker areas means porous zones.

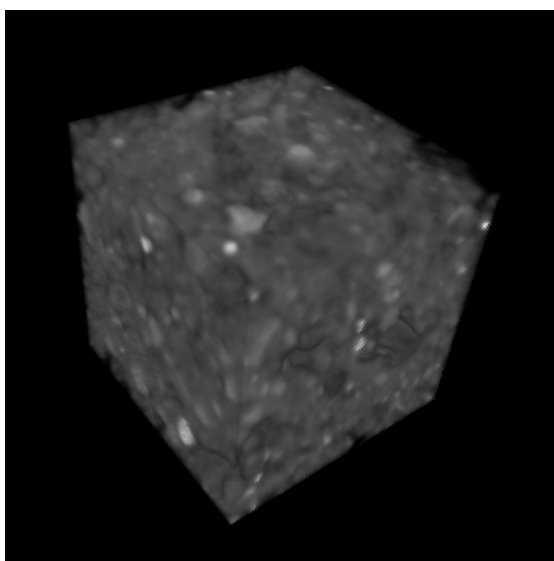


Figure 5.1: 3 Dimensional model reconstructed from soil aggregates sample.

5.1.1 Two-dimensional analysis

In order to have a first estimation of the structure with a low computing cost, we have studied different 2 dimensional slices. We have selected 3 slices uniformly distributed along each 3 main direction of the space. They can be seen in Figure 5.2.

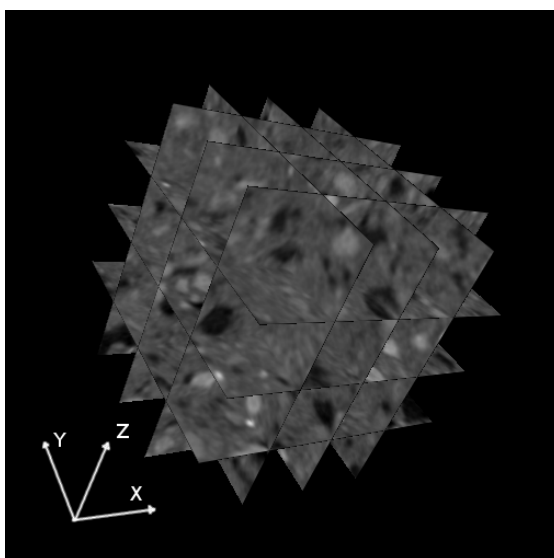


Figure 5.2: Model reconstructed with 3 slices of each main direction.

The computing time in 2 dimensional models is very low, so it can give a first measure about the multifractal structure of the samples. Here we have slices of 260x260 px and 260x256 px so for the box counting method they have been resized to 256x256 px. In the Gliding method the original size of the images have been used. Then the results for the XY, YZ and XZ planes are shown.

First we compute $\tau(q)$ for each slice in the plane XY (Figure 5.3), then D_q (Figure 5.4) and derived the $\alpha(q)$ (Figure 5.5).

For each of the planes XY, XZ, YZ we will follow this order. Therefore, plane XZ analysis is from Figure 5.7 till Figure 5.10, and plane YZ is from Figure 5.11 till Figure 5.14

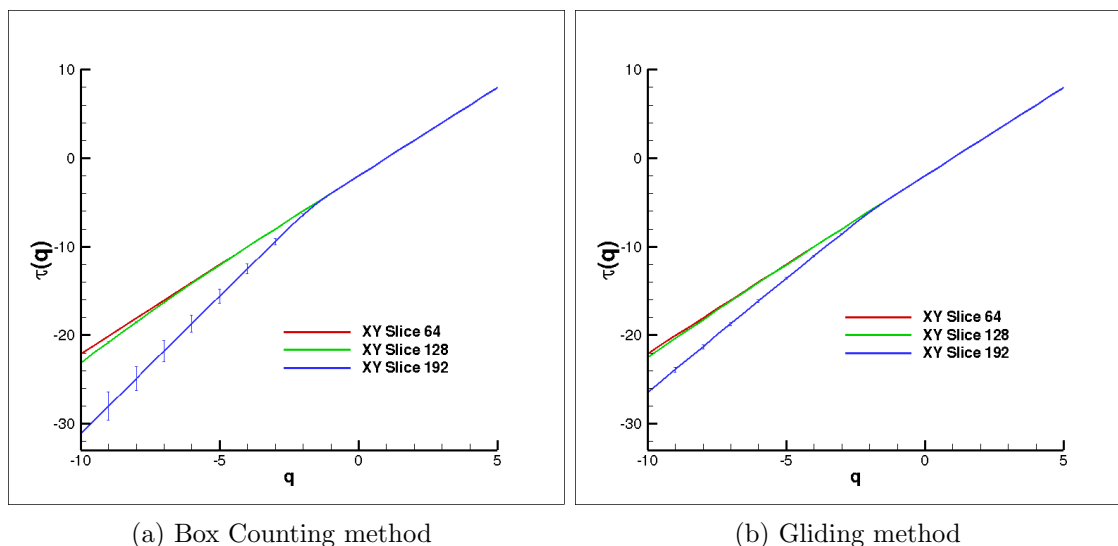


Figure 5.3: $\tau(q)$ for some slices of plane XY.

Comparing Box Counting method and Gliding method the errors in $\tau(q)$ diminished in the negative q values as it is relevant in slice 192. On the other hand, slice 64 and 128 present similar structure meanwhile 192 is significantly different. The curvature of $\tau(q)$ is smoother in the Gliding method. However the differences are retained.

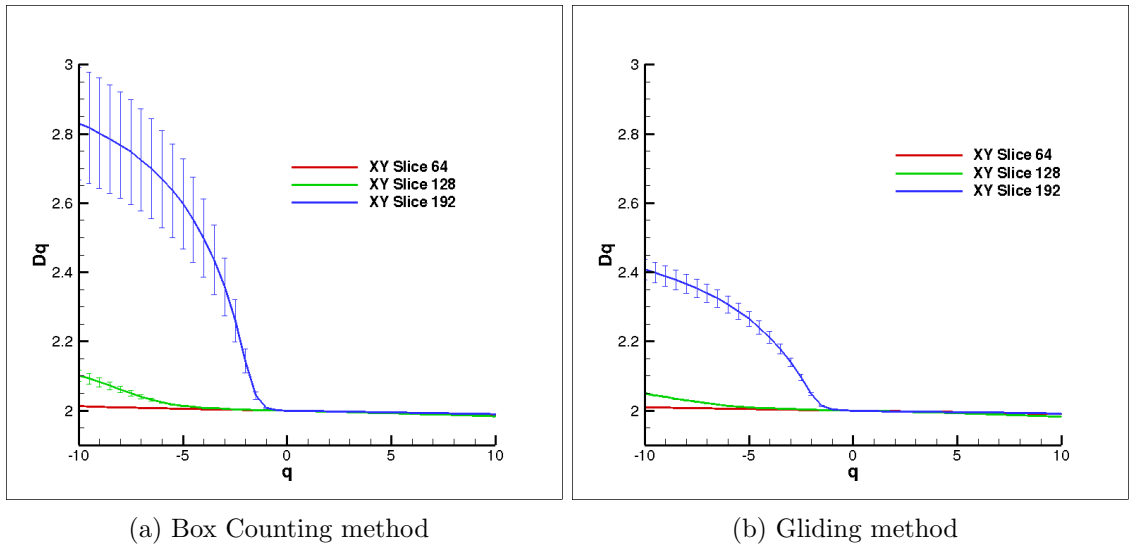


Figure 5.4: D_q for some slices of plane XY.

D_q shows the same results as $\tau(q)$ it is derivative from there. For negative q values the differences are more clear between slice 128 and slice 64.

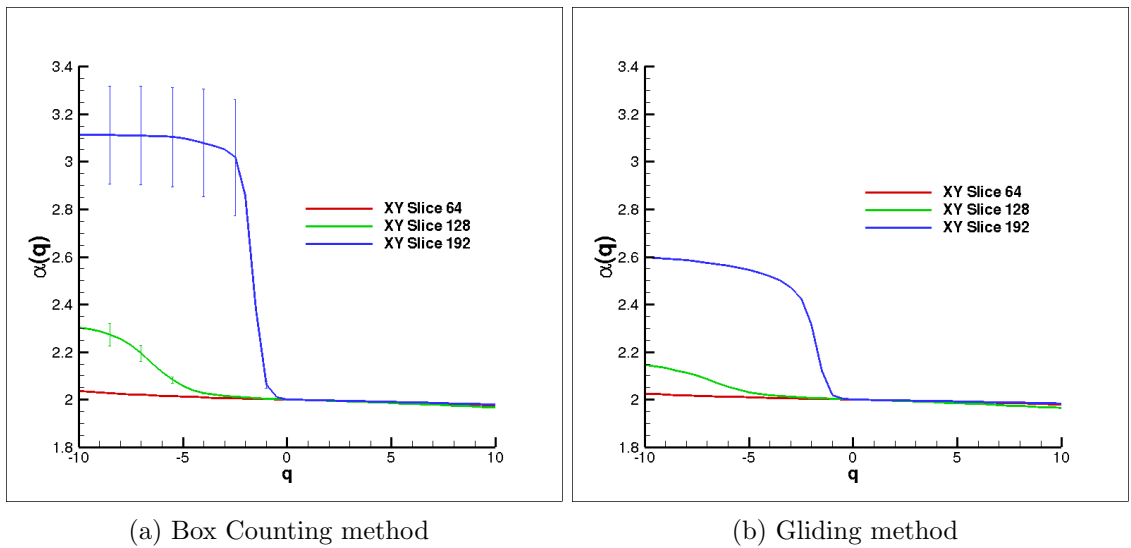
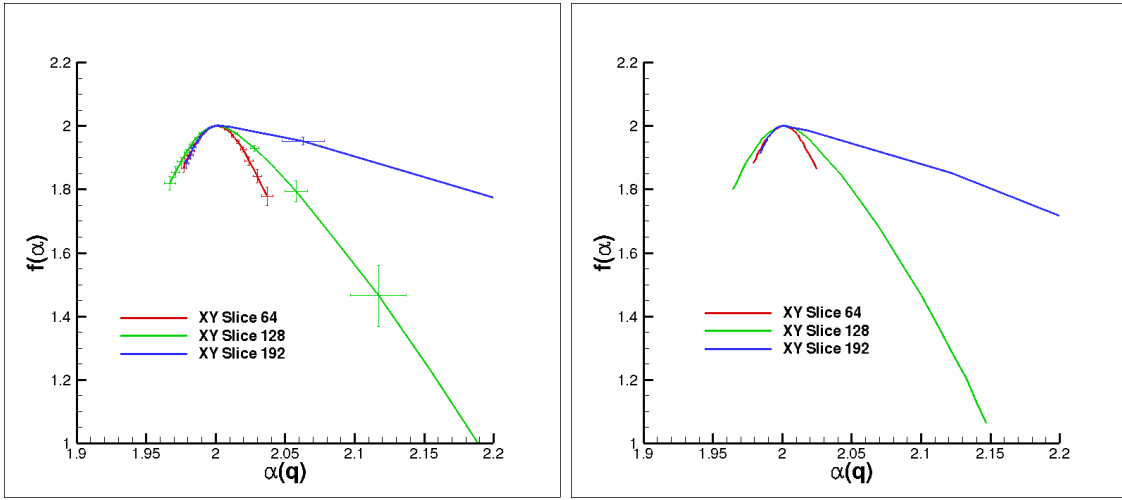


Figure 5.5: $\alpha(q)$ for some slices of plane XY.

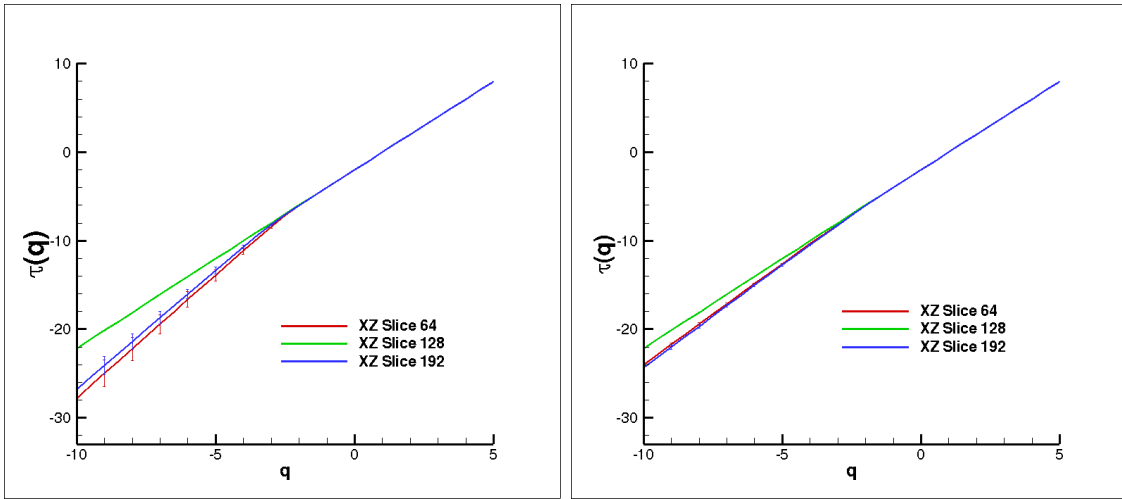
The same conclusions are achieved observing $\alpha(q)$ behaviour.



(a) Box Counting method (b) Gliding method

Figure 5.6: Multifractal spectrum $f(\alpha)$ for some slices of plane XY.

The multifractal spectrum gives us a complete information in the hierarchical soil structure. Slice 64 shows a weak multifractal character in concordance with previous results. Slice 128 presents a strong scaling in the low values, being stronger in slice 192.



(a) Box Counting method (b) Gliding method

Figure 5.7: $\tau(q)$ for some slices of plane XZ.

At the XZ plane, slices 64 and 192 presents similar structure with more multifractal behaviour than slice 128.

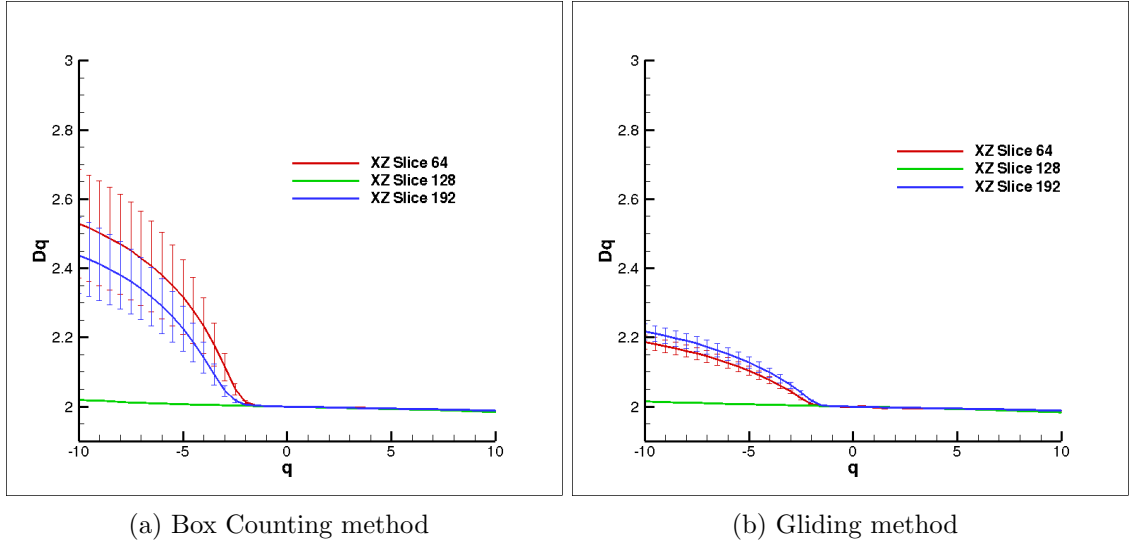


Figure 5.8: D_q for some slices of plane XZ.

In the D_q measures the values of slices 64 and 192 are very similar. They can not be differentiated as the error bars overlap themselves.

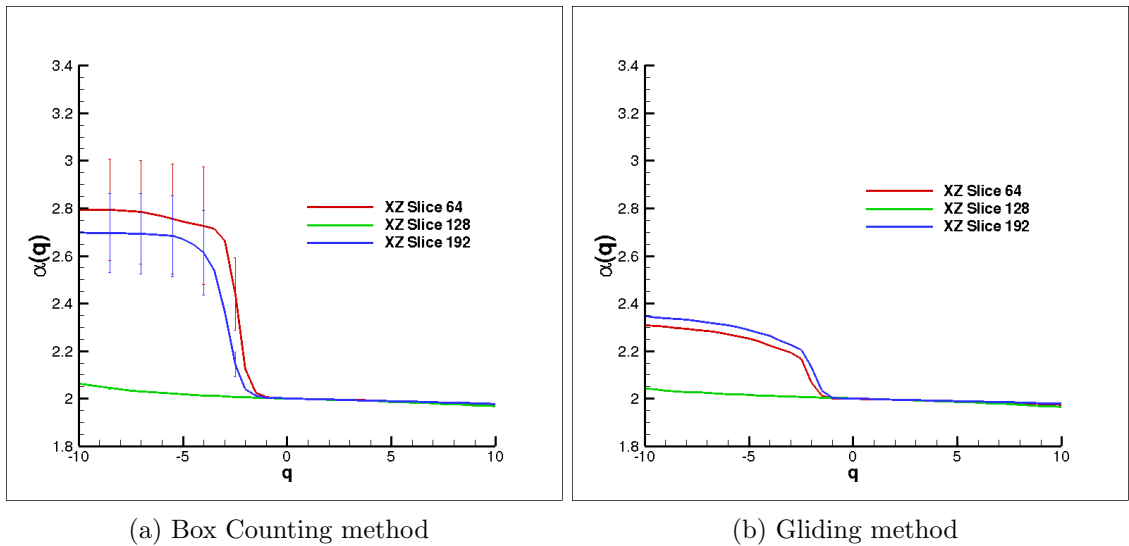


Figure 5.9: $\alpha(q)$ for some slices of plane XZ.

As in the previous Figures slices 64 and 192 can not be differentiated and slice 128 presents a weak multifractal behaviour.

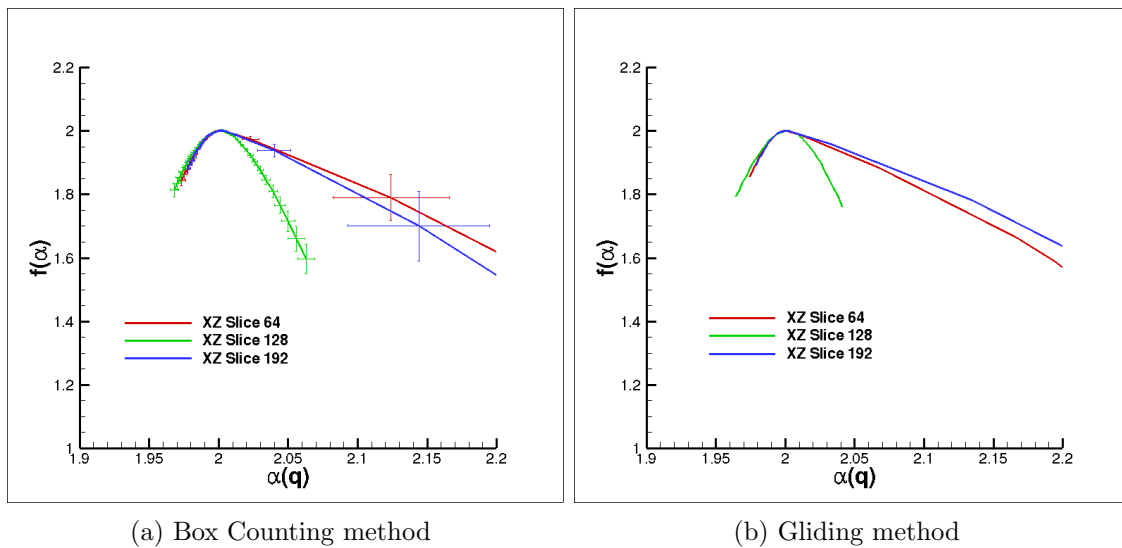
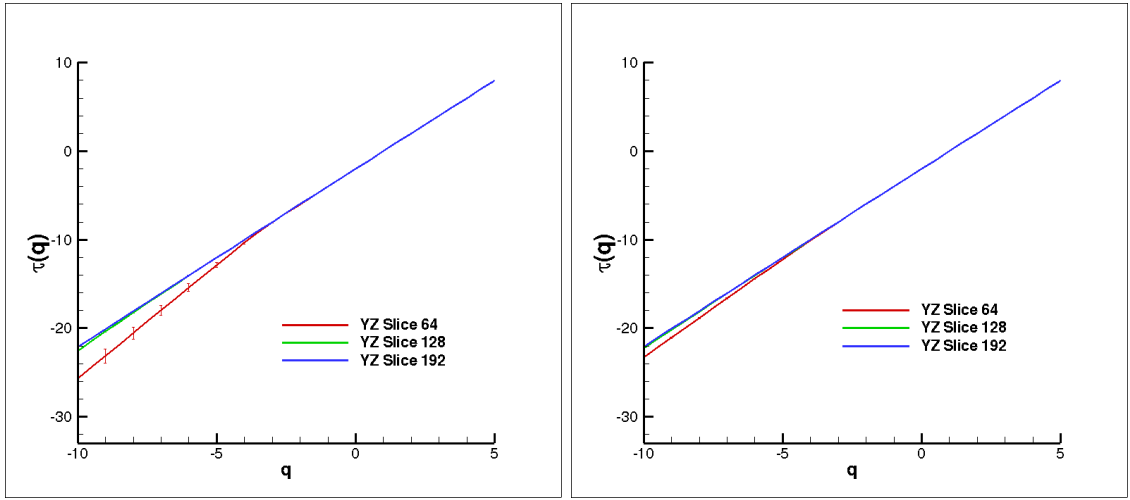


Figure 5.10: Multifractal sepectrum $f(\alpha)$ for some slices of plane XZ.

Slice 128 shows a mild multifractal spectrum in the concordance with previous results.

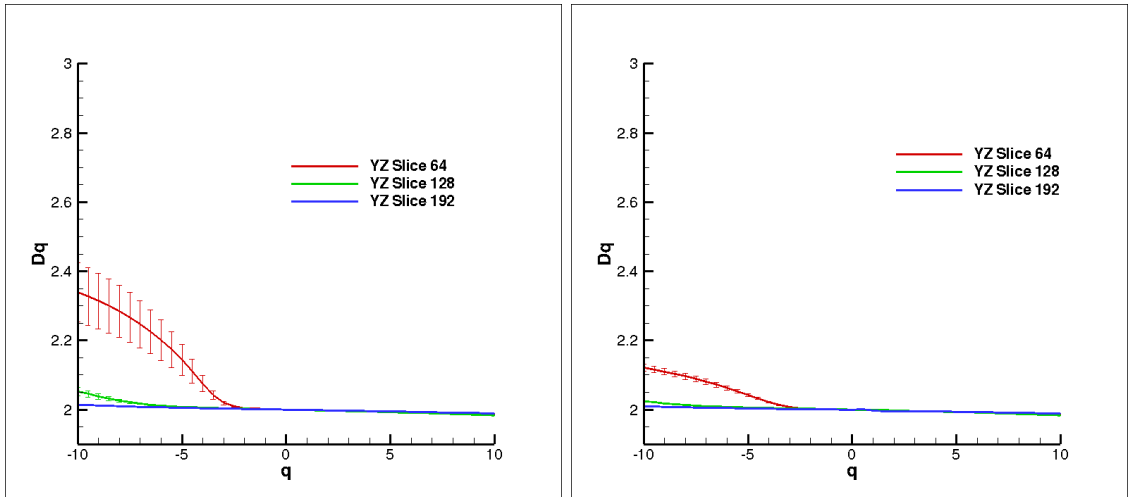
Basically, the results in the slices at YZ are the same than in the slices at XY plane. However in this case the slice 64 is the one that is differentiated from the other ones.



(a) Box Counting method

(b) Gliding method

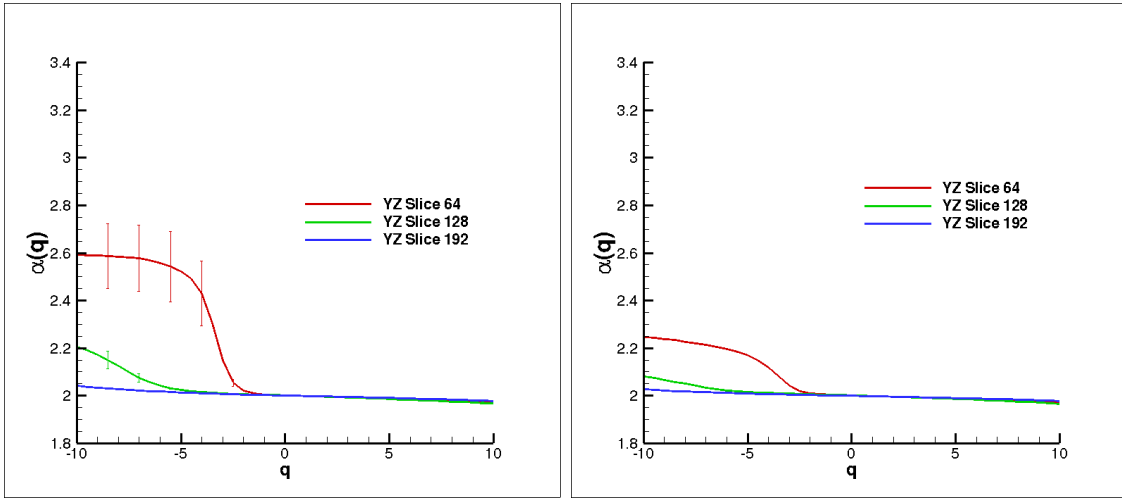
Figure 5.11: $\tau(q)$ for some slices of plane YZ.



(a) Box Counting method

(b) Gliding method

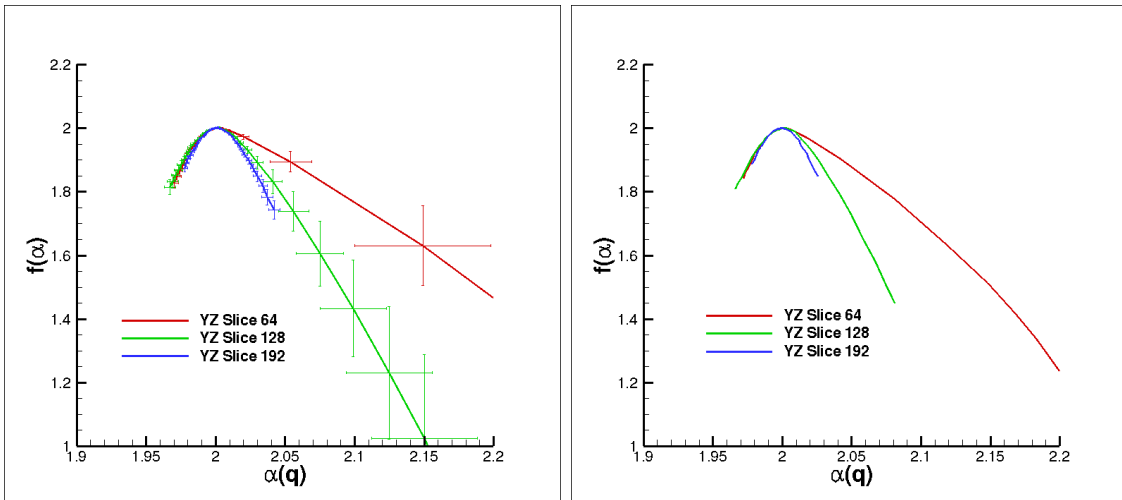
Figure 5.12: D_q for some slices of plane YZ.



(a) Box Counting method

(b) Gliding method

Figure 5.13: $\alpha(q)$ for some slices of plane YZ.



(a) Box Counting method

(b) Gliding method

Figure 5.14: Multifractal spectrum $f(\alpha)$ for some slices of plane YZ.

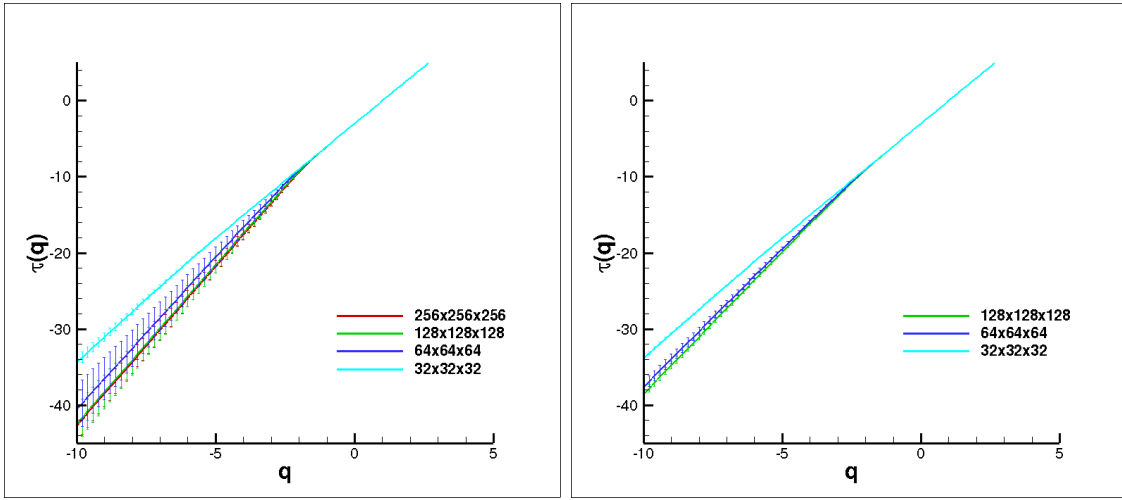
Multifractal spectrum gives again a better inside information pointing out the hierarchical strength among the slices. The scaling behaviour is smoother in the negative q values in the case of Gliding method.

As seen in the previous Figures there are differences between the slices results from the same and different planes, specially between the slices of plane XY along Z direction. This implies that the greatest changes in the structure of the soil occurred in the gravity normal direction to the surface. In this direction take place the main natural processes such as sedimentation, filtration among others. Consequently trying to understand the soil complexity only studying it as a bidimensional structure does not reflect all of it. For reaching all the complexity it must be studied as a whole 3-dimensional system. This is what has been done in the following section.

Note that for the positive q values Gliding and Box Counting method gives very similar results while for the negative ones are very different. One reason is because the box counting method has great errors in the low density areas. Beside this, at Box Counting method the slices has been resized coarsing the structure.

5.1.2 Three-dimensional analysis

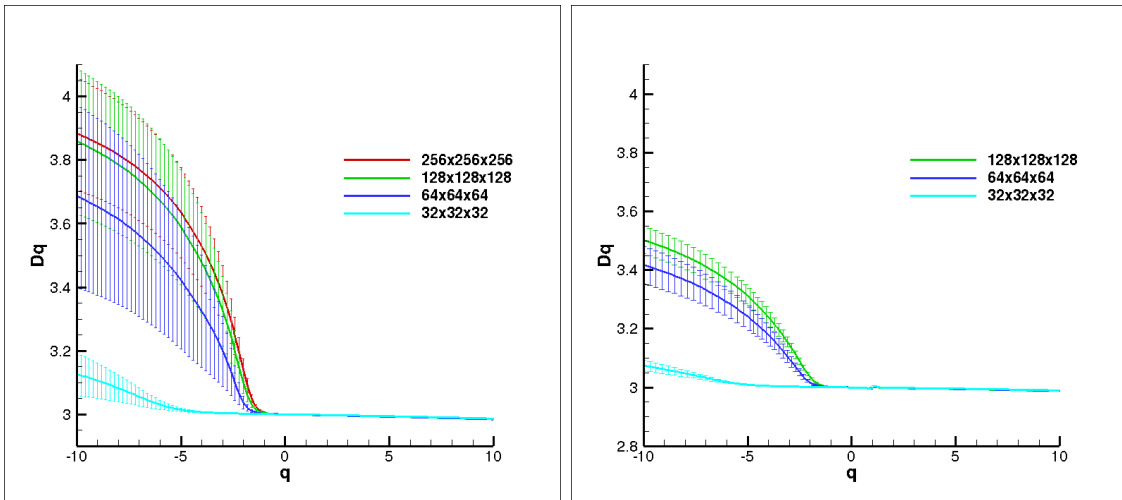
In this section we have computed the full 3 dimensional model of the soil. Due to the high computation time required in the study of 3 dimensional structure we have resized several times the model for comparing the time required and the validity of the results. They are also employed the box counting and gliding methods. We do not have computed the 256x256x256 voxel through gliding method because of the high computing time required estimated in one month.



(a) Box Counting method

(b) Gliding method

Figure 5.15: $\tau(q)$ for 3D model.



(a) Box Counting method

(b) Gliding method

Figure 5.16: D_q for 3D model.

General results follows the same comments given in the earlier section. We can point out that for negative q values are highly sensitive to an upscaling size. From 256x256x256 voxel till 128x128x128 the results for $\tau(q)$, D_q , $\alpha(q)$ and $f(\alpha)$ in the

Box Counting method are similar. In the 64x64x64 size a tendency to reduce a multifractal behaviour is shown. This is clear in 32x32x32 case.

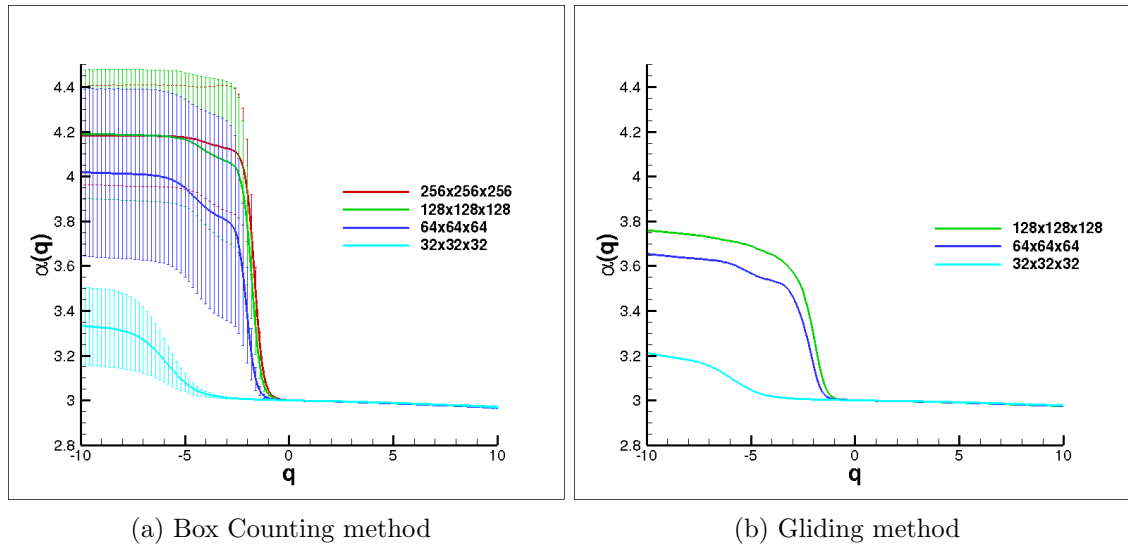


Figure 5.17: $\alpha(q)$ for 3D model.

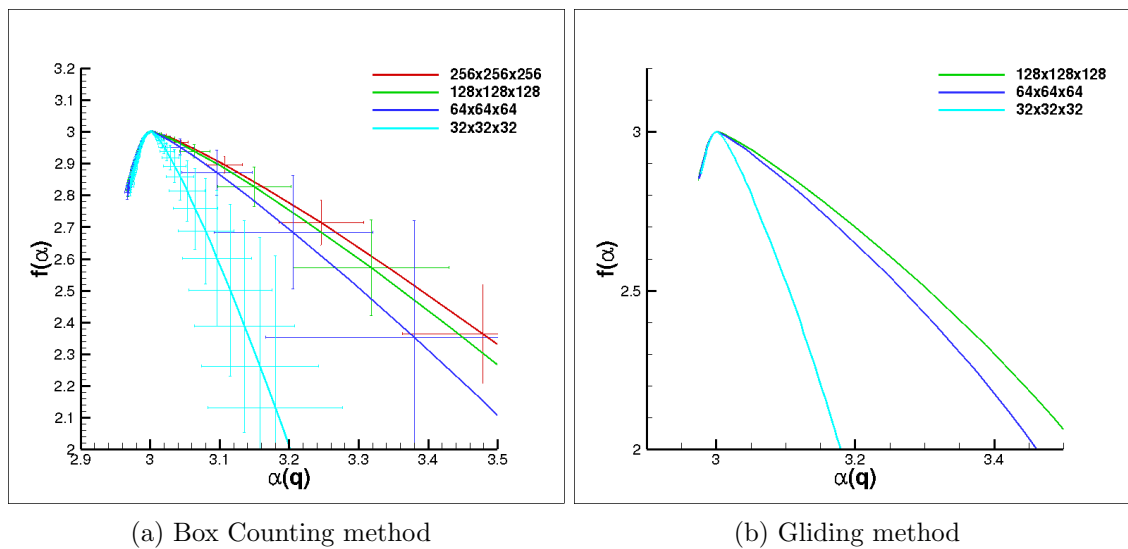


Figure 5.18: Multifractal spectrum $f(\alpha)$ for 3D model.

In the Gliding method the significant differences are found between 128x128x128 and 64x64x64 sizes compared to 32x32x32.

The high errors in negative q values are mainly because because we have used all $X(q)$ for getting D_q , α and $f(\alpha)$. In most of cases they could have been reduced by adjusting with more accuracy $X(q)$ shown in Appendix A

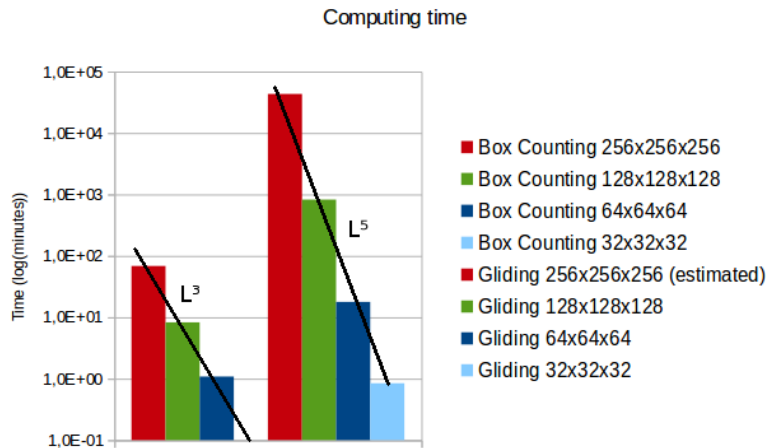


Figure 5.19: Computing times for the different sizes and methods of 3D images. The trend line shows the expected computing time where L is the characteristic dimension, e.g. 256, 128.

As seen in Figure 5.19 the computing time get higher very quickly with the size of the slices (note that the y-axis is shown in logarithmic scale). After 15 days of calculations the 256x256x256 voxel in gliding method was in the middle of the calculus, so it is estimated that it would cost up to 30 days to finalize. The computing time of 32x32x32 voxel with box counting method is so low that can not be appreciated properly in the picture. It seems that the computing time and the size of the sample are related with a power law function. This means that a small increment of the size to be analysed increments highly the computing time.

5.2 Tillage treatments

The trials were conducted at the Alameda del Obispo experimental farm (38N, 5W, altitude 110m), Cordoba, Spain (see Figure 5.20). The climate is Mediterranean with a mean annual rainfall of 595mm. Summer in Cordoba is dry and hot while autumn and winter are mild and rainy [15]. The soil is a loamy alluvial with

particle-size distribution in the upper (0-15 cm) soil layer: sand, $350 \frac{g}{kg}$; silt, $443 \frac{g}{kg}$; and clay $207 \frac{g}{kg}$ [16].

Soil samples for each of the tillage treatment were packed into polypropylene cylinders of 8 cm diameter and 10 cm high. These were imaged using an mSIMCT at 155keV and 25 mA. An aluminium filter (0.25 mm) was applied to reduce beam hardening and later several corrections were applied during reconstruction. All 3D volumes were converted using VGStudioMax v.1.2.1 into image stacks with voxel-thick slices.

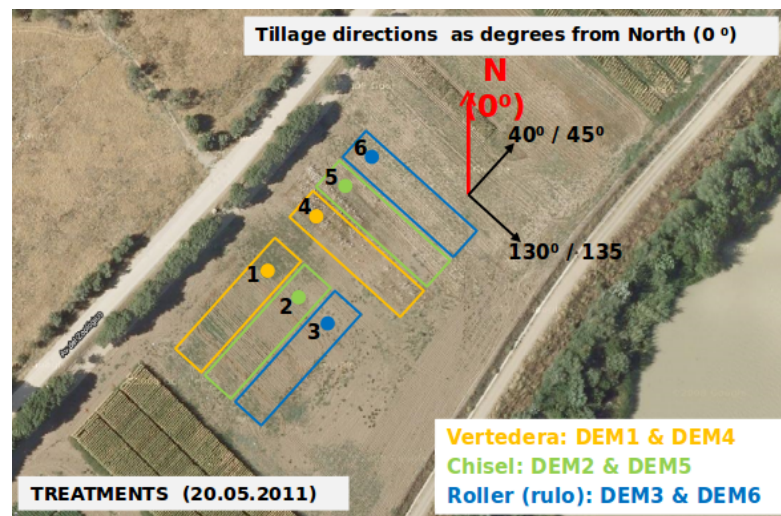


Figure 5.20: Soil samples were extracted from different areas plowed with three different tools: moldboard(vertedera) in yellow, chisel in green and roller in blue.

As in the previous section we have already seen that the 2 dimensional analysis is not enough for showing the complexity of the soil, here we have analyzed directly the 3 dimensional model. For this purpose we have selected a $256 \times 256 \times 256$ voxel piece from the full sample. Taking into account a reasonable computing time and good precision of the calculus with the available computer we have analysed that piece with box counting method and then, resizing it to $128 \times 128 \times 128$ voxel for the analysis both with gliding and box counting method. Then results are shown for each type of plowing technique.

5.2.1 Moldboard

In Figure 5.21 shows the original 3-Dimensional model reconstructed from the slices obtained with CT-scan. Due to the big size of the sample (more than $700 \times 800 \times 256$ voxel) it would not be possible to compute it in a reasonable time with a standard computer. Therefore, we have selected a $256 \times 256 \times 256$ voxel subsample for the analysis. First the full size with the box counting method, and then scaling it to $128 \times 128 \times 128$ voxel and analysing both with box counting and gliding methods. These procedure is the same for the chissel (Figure 5.26) and roller samples (Figure 5.31).

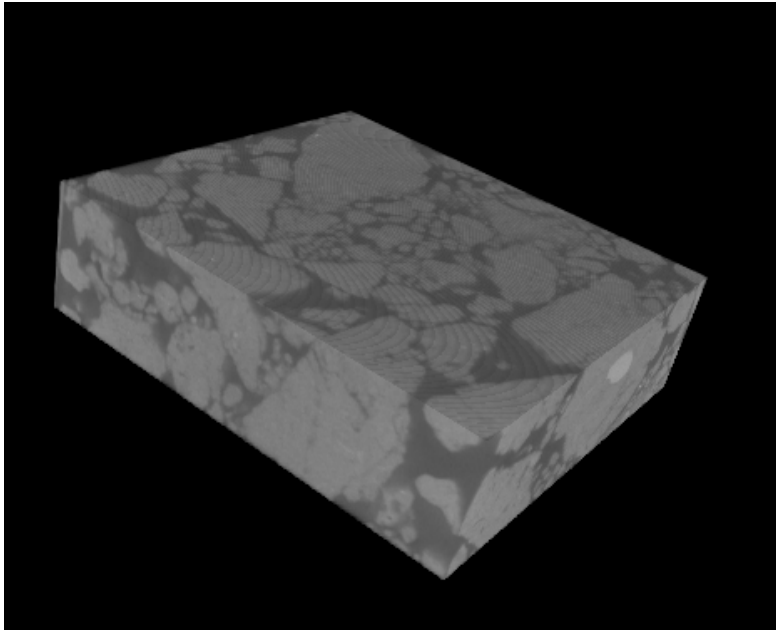


Figure 5.21: Original 3D model from moldboard sample.

In Figures 5.22, 5.23, 5.24, 5.25 are shown the results of the multifractal analysis.

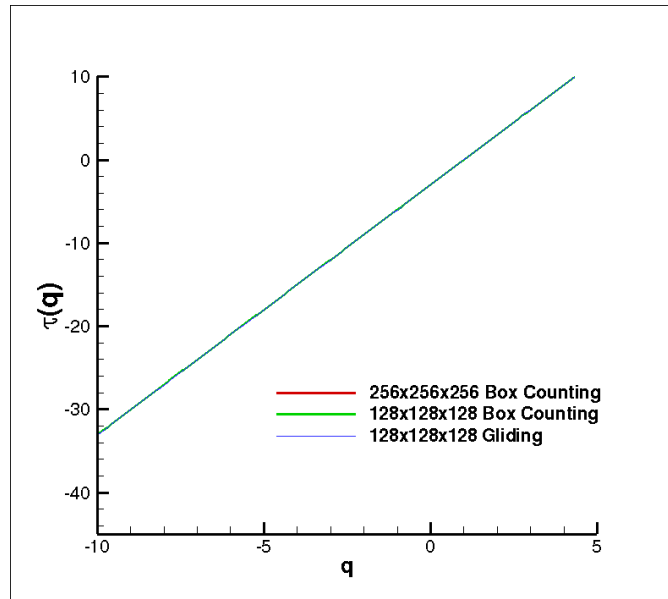


Figure 5.22: $\tau(q)$ of 3D moldboard sample.

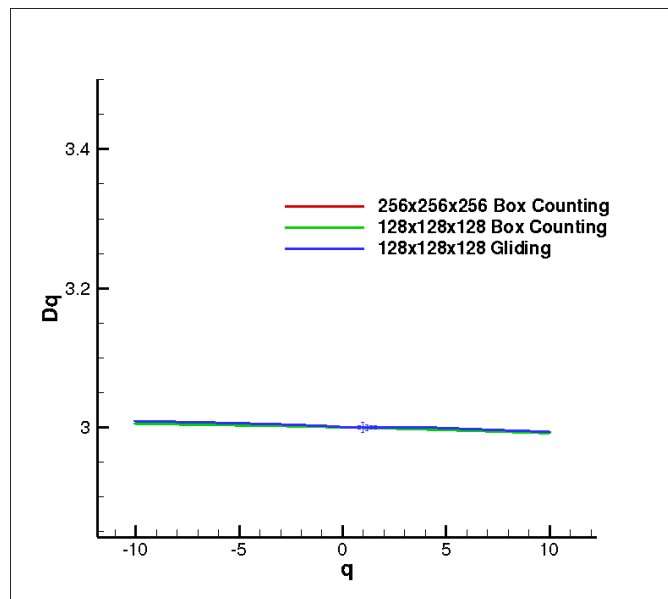


Figure 5.23: D_q of 3D moldboard sample.

As seen in Figures 5.22 and 5.23 there are not differences between teh sizes and methods used. The sample shows a weak multifractal behaviour as D_q values

are very similar for each q . Besides the errors are so low that can not be appreciated in the Figures.

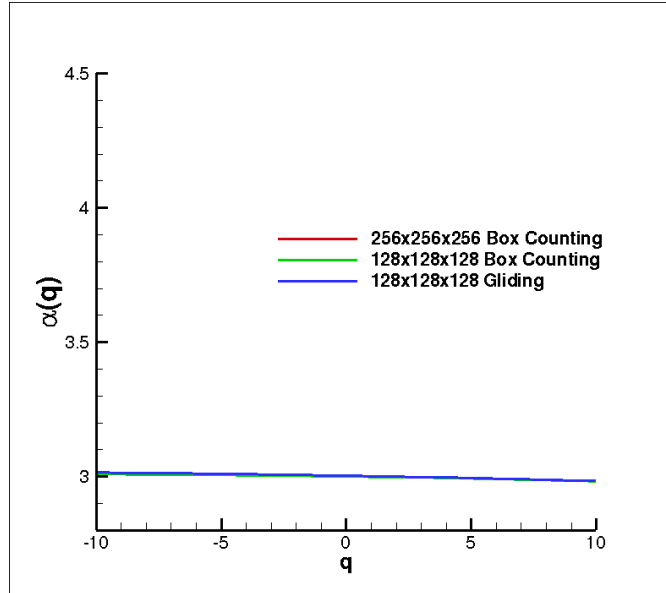


Figure 5.24: $\alpha(q)$ of 3D moldboard sample.

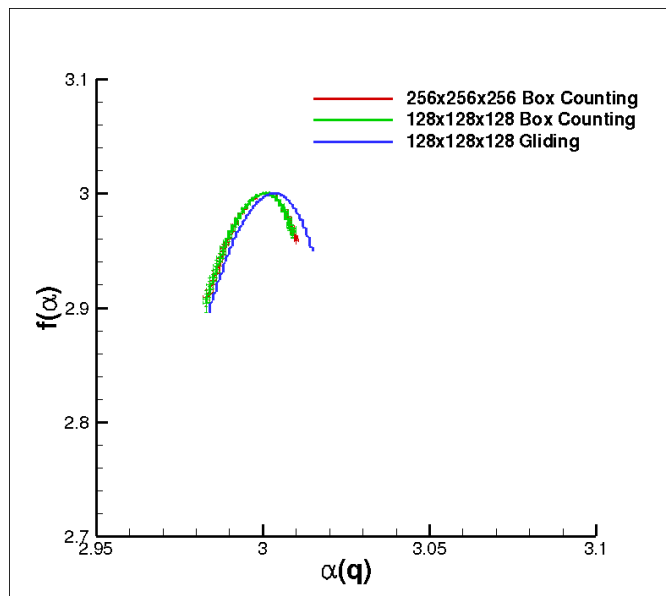


Figure 5.25: $f(\alpha)$ of 3D moldboard sample.

Finally as be expected the multifractal spectrum is very similar for each size and method, although there are some differences for the Gliding method. In this case there would not be any advantage for using big samples or Gliding method which would demand more computing time.

5.2.2 Chissel

In Figure 5.26 can be appreciated structure differences in comparison with Figure 5.21

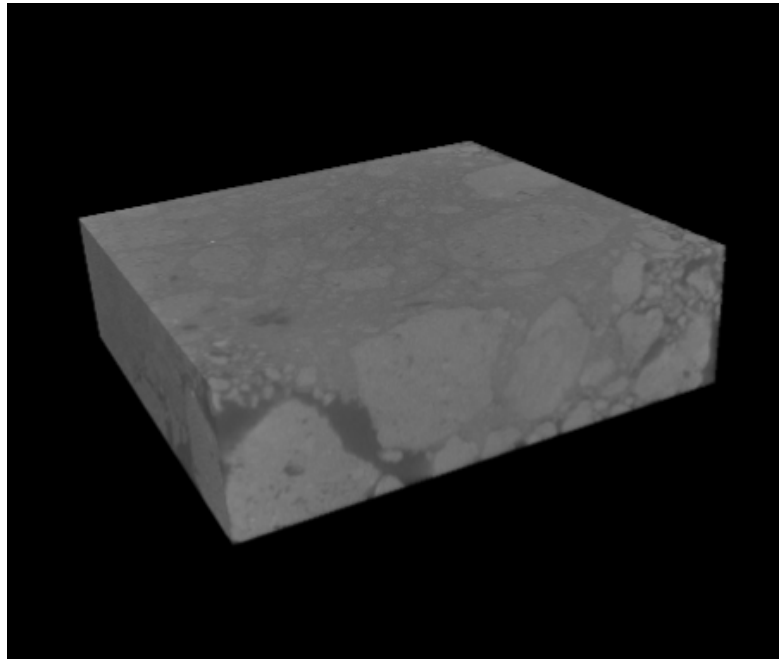


Figure 5.26: Original 3D model from chissel sample.

Then in Figures 5.27, 5.28, 5.29, 5.30 are shown the results from the multifractal analysis of the Chisel soil sample.

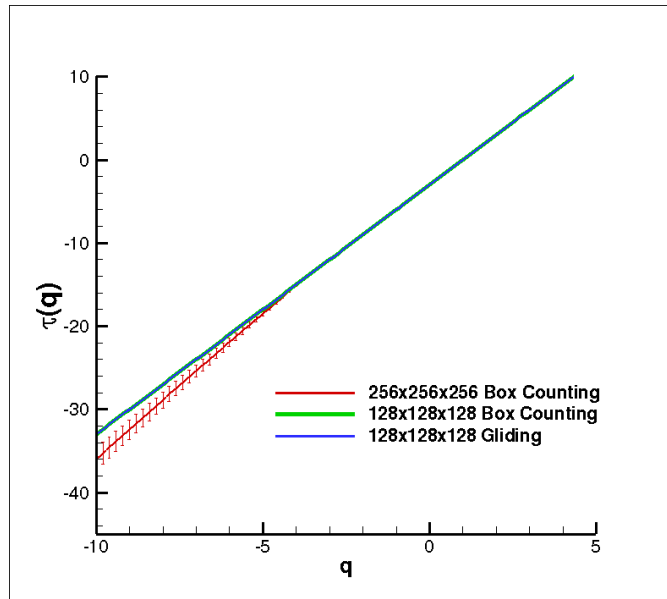


Figure 5.27: $\tau(q)$ of 3D chissel sample.

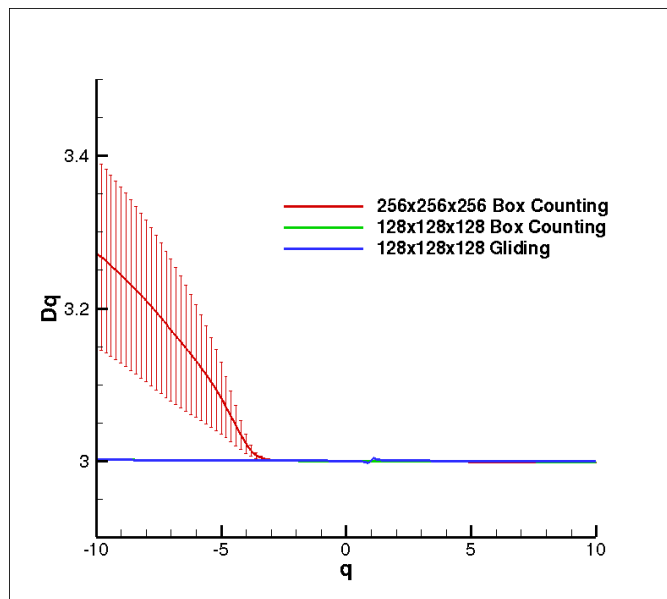


Figure 5.28: Dq of 3D chissel sample.

In this case there difference between 128 and 256 sizes. At 128 size there is no difference between Gliding and Box Counting method.

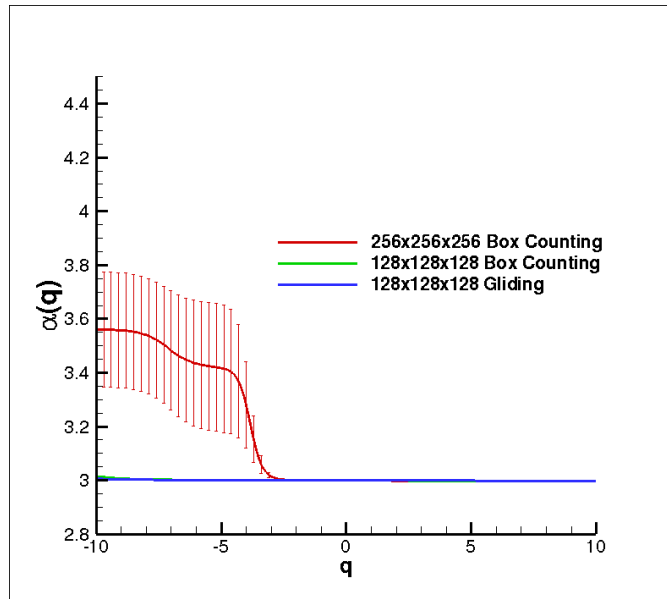


Figure 5.29: $\alpha(q)$ of 3D chissel sample

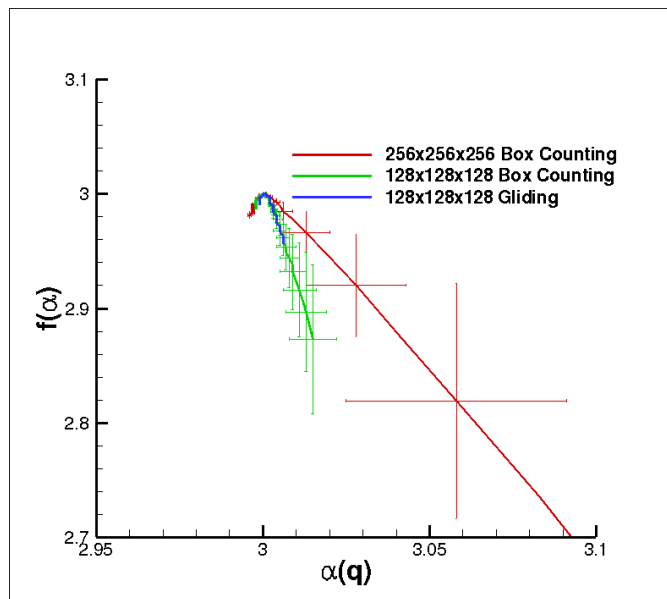


Figure 5.30: $f(\alpha)$ of 3D chissel sample.

In Chissel case it shows that using smaller samples would not show properly the multifractal generalized dimensions.

5.2.3 Roller

Finally in Figure 5.31 is shown the full piece of soil plowed with roller tillage. As in the previous cases, a 256x256x256 voxel three-dimensional view is extracted from the full sample for the analysis.

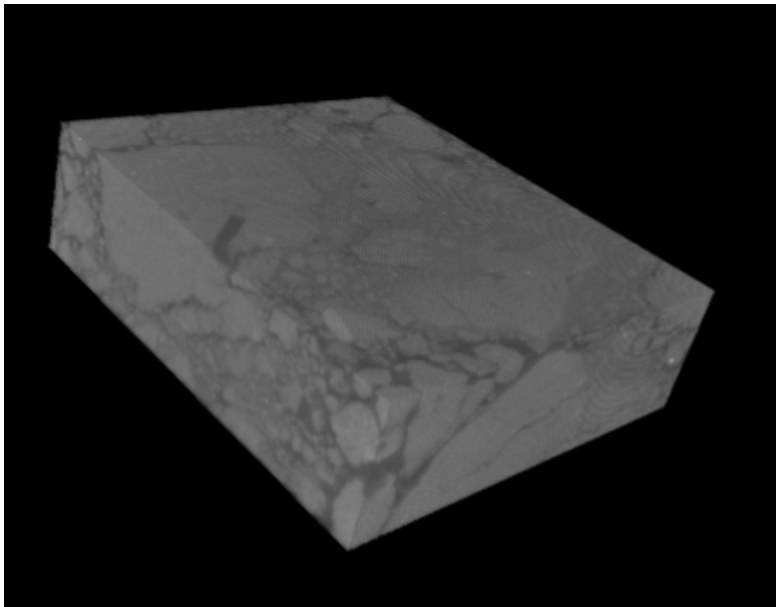


Figure 5.31: Original 3D model from roller sample.

Roller soil sample is analyzed and the results shown in Figures 5.32, 5.33, 5.34, 5.35.

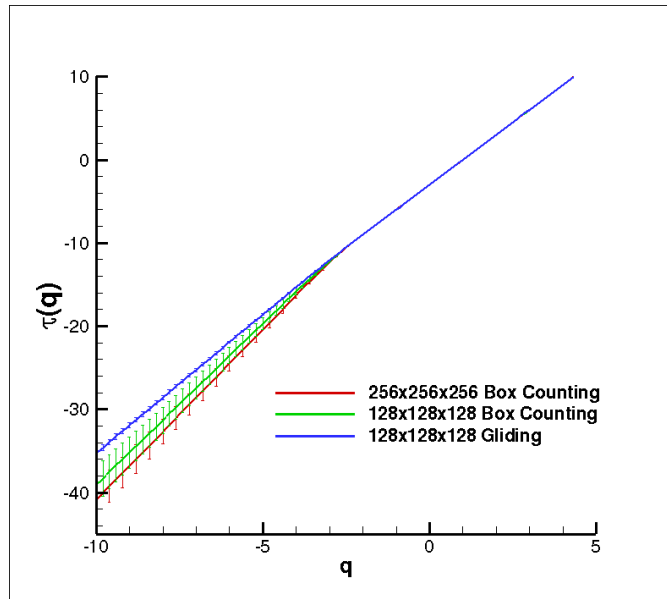


Figure 5.32: $\tau(q)$ of 3D roller sample.

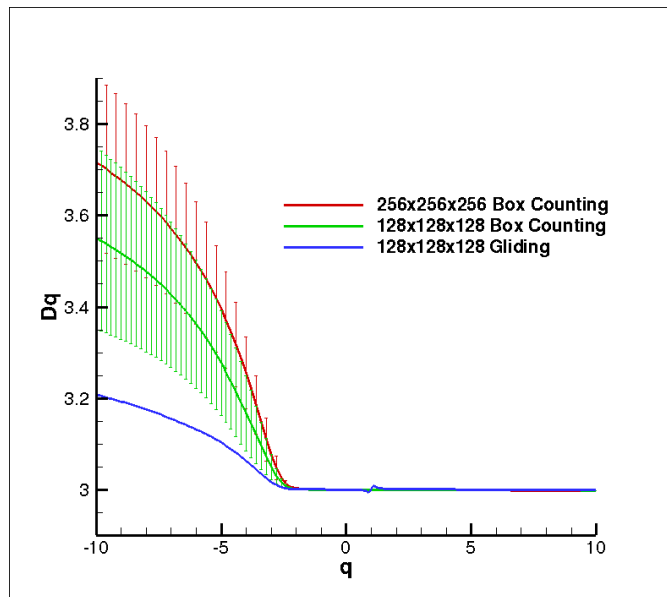


Figure 5.33: D_q of 3D roller sample.

In this case the values obtained through 256x256x256 voxel and 128x128x128 voxel can not be differentiated because their errors includes themselves. Meanwhile Gliding method shows smoother curve that Box Counting method.

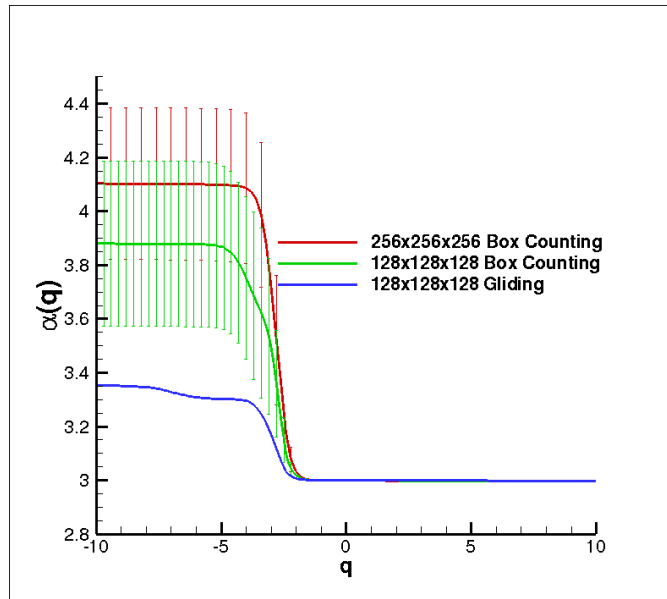


Figure 5.34: $\alpha(q)$ of 3D roller sample.

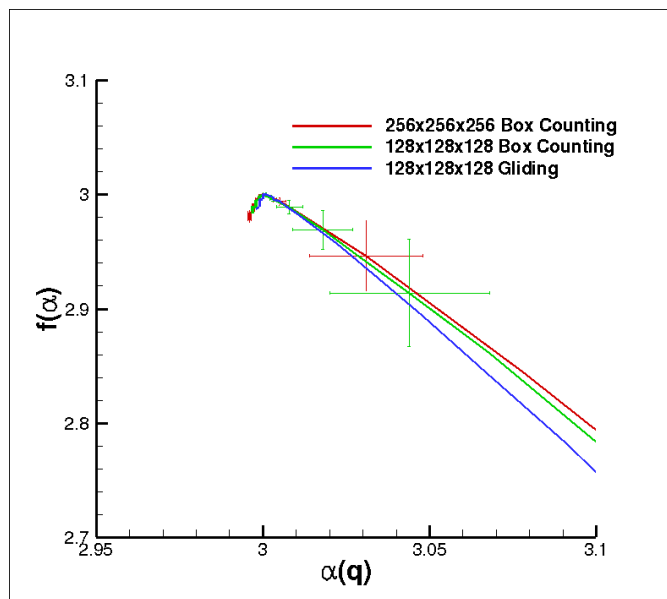


Figure 5.35: Multifractal spectrum $f(\alpha)$ of 3D roller sample.

Although in Figures 5.32, 5.33, 5.34 there are several differences between Box Counting and Gliding method, those are reduced in the multifractal spectrum of Figure 5.35

5.2.4 Multifractal comparison

Finally we have selected the results from 256x256x256 voxel in Box Counting from the three tillage methods and compared them in Figure 5.36

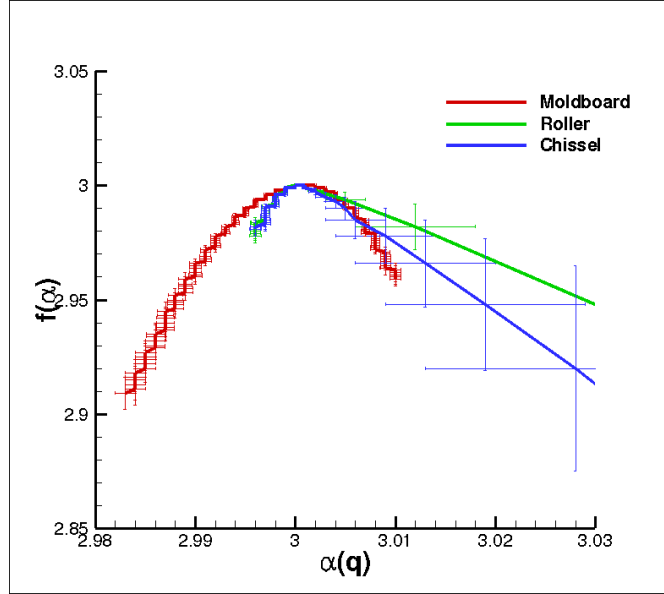


Figure 5.36: Multifractal spectrum of Moldboard, Roller and Chissel tillage for Box Counting method and 256x256x256 voxel samples.

The comparison of multifractal spectrum shows that Chissel and Roller tillage scales similarly. Moldboard tillage scales for positive q values while Chissel and Roller do for negative q values. The several differences for q positive values are detailed in table 5.1.

Method	Box Counting						Gliding		
Resolution	256			128			128		
Sample	M	R	C	M	R	C	M	R	C
α_{min}	2.983	2.996	2.996	2.983	2.997	2.998	2.984	2.998	2.999
$f(\alpha_{min})$	2.909	2.984	2.982	2.910	2.989	2.995	2.903	2.988	2.997

Table 5.1: $f(\alpha_{min})$ and α_{min} values for each method and size.

Respect to the role of each tillage tool in the hierarchy of soil's structure,

Moldboard creates a higher complexity in the soil aggregates as physically removes the soil. Chisel and Roller tends to destruct the aggregates reducing the soil rugosity.

Chapter 6

Conclusions

3-Dimensional images were obtained from four different soil samples. In order to describe and characterize the porosity structure we have studied their generalized fractal and multifractal dimension through gliding and box counting methods. Gliding method gives results which trends soft functions and few errors, while the box counting method gives results faster but with more errors. The computing time in 3-D images is related with a power law function of the characteristic dimension of the piece. This is very critical in Gliding method where with a i-7 processor would need one month for calculating the multifractal spectrum of a 256x256x256 voxel sample.

Slices from the 3 main directions of the 3D sample were extracted and analysed. The great variations were found between parallel planes trough the surface normal direction. This has sense because in this direction take place the main natural processes, e.g. sedimentation, filtration which change the porosity structure of the soil. However studying the soil structure using two dimensional planes is not enough for showing the complexity it has, a 3-D analysis is needed.

Reducing the images for analyse their structure saving computing time yields good results when doing this one or two times, e.g: from 256x256x256 voxel to 128x128x128 voxel or even to 64x64x64 voxel. But reducing further the samples alters too much the original structure.

Finally soil samples plowed with different techniques were analyzed. The multifractal spectrum comparison shown several differences between one of them and the other two ones. Moldboard tillage shows a high complexity for positive q val-

ues as physically it removes the soil. Meanwhile the other two tillages are very similar and shows less complexity for positive q values as they physically tends to destruct the aggregates reducing the soil rugosity.

Bibliography

- [1] D. Powlson, “Climatology: Will soil amplify climate change?,” *Nature*, vol. 433, no. 7023, pp. 204–205, 2005.
- [2] I. M. Young and J. W. Crawford, “Interactions and self-organization in the soil-microbe complex,” *Science*, vol. 304, no. 5677, pp. 1634–1637, 2004.
- [3] A. Tarquis, R. Heck, J. Grau, J. Fabregat, M. Sanchez, and J. Antón, “Influence of thresholding in mass and entropy dimension of 3-d soil images.,” *Nonlinear Processes in Geophysics*, vol. 15, no. 6, 2008.
- [4] Y. Pachepsky, D. E. Radcliffe, and H. M. Selim, *Scaling methods in soil physics*. CRC press, 2004.
- [5] B. B. Mandelbrot, “How long is the coast of britain,” *Science*, vol. 156, no. 3775, pp. 636–638, 1967.
- [6] B. B. Mandelbrot, *The fractal geometry of nature*. Macmillan, 1983.
- [7] B. B. Mandelbrot, “Intermittent turbulence in self-similar cascades: divergence of high moments and dimension of the carrier,” in *Multifractals and 1/Noise*, pp. 317–357, Springer, 1999.
- [8] D. A. Russell, J. D. Hanson, and E. Ott, “Dimension of strange attractors,” *Physical Review Letters*, vol. 45, pp. 1175–1178, 1980.
- [9] C. Meneveau and K. Sreenivasan, “Simple multifractal cascade model for fully developed turbulence,” *Physical Review Letters*, vol. 59, no. 13, p. 1424, 1987.

- [10] H. T. Teng, H.-T. Ewe, and S. L. Tan, “Multifractal dimension and its geometrical terrain properties for classification of multi-band multi-polarized sar image,” *Progress In Electromagnetics Research*, vol. 104, pp. 221–237, 2010.
- [11] A. Chhabra and R. V. Jensen, “Direct determination of the $f(\alpha)$ singularity spectrum,” *Physical Review Letters*, vol. 62, no. 12, pp. 1327–1330, 1989.
- [12] Q. Cheng, “The gliding box method for multifractal modeling,” *Computers & Geosciences*, vol. 25, no. 9, pp. 1073–1079, 1999.
- [13] J. Grau, V. Méndez, A. Tarquis, M. Díaz, and A. Saa, “Comparison of gliding box and box-counting methods in soil image analysis,” *Geoderma*, vol. 134, no. 3, pp. 349–359, 2006.
- [14] S. Favretto, *Applicatinos of X-ray computed microtomography to material science: decices and perspectives*. Universit degli studi di trieste, 2008.
- [15] M. C. Peel, B. L. Finlayson, and T. A. McMahon, “Updated world map of the köppen-geiger climate classification,” *Hydrology and earth system sciences discussions*, vol. 4, no. 2, pp. 439–473, 2007.
- [16] H. Boulal, H. Gómez-Macpherson, J. A. Gómez, and L. Mateos, “Effect of soil management and traffic on soil erosion in irrigated annual crops,” *Soil and Tillage Research*, vol. 115, pp. 62–70, 2011.

Appendices

Appendix A

$X(q, \epsilon)$ list of 2D slices of soil aggregates sample calculated with different methods

Then there are the values of $X(q, \epsilon)$ from which are obtained the values of τ , α and $f(\alpha)$. The values are for each 3 slices selected of each main direction of the 3 dimensional model.

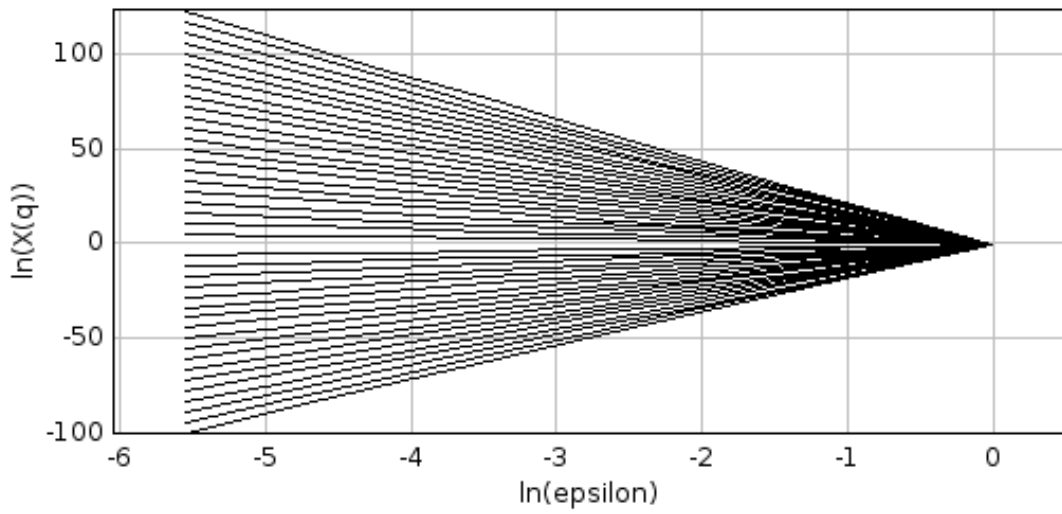


Figure A.1: $X(q, \epsilon)$ of the slice 64 from XY plane obtained through Box Counting method

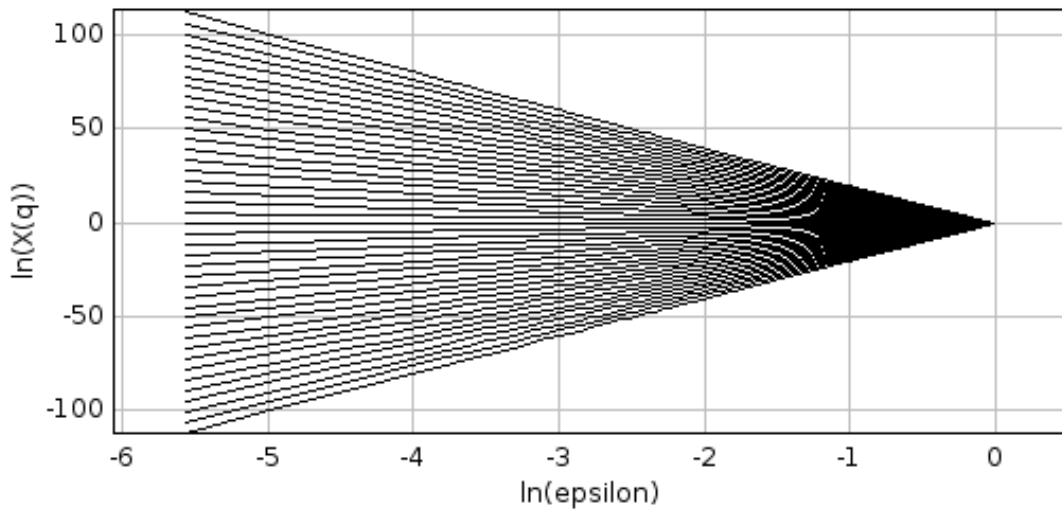


Figure A.2: $X(q, \epsilon)$ of the slice 64 from XY plane obtained through Gliding method

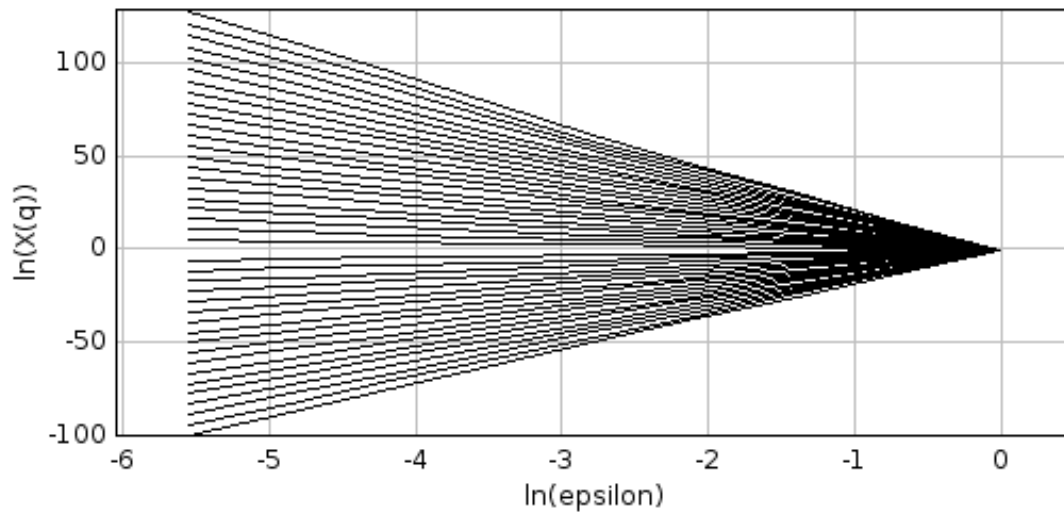


Figure A.3: $X(q, \epsilon)$ of the slice 128 from XY plane obtained through Box Counting method

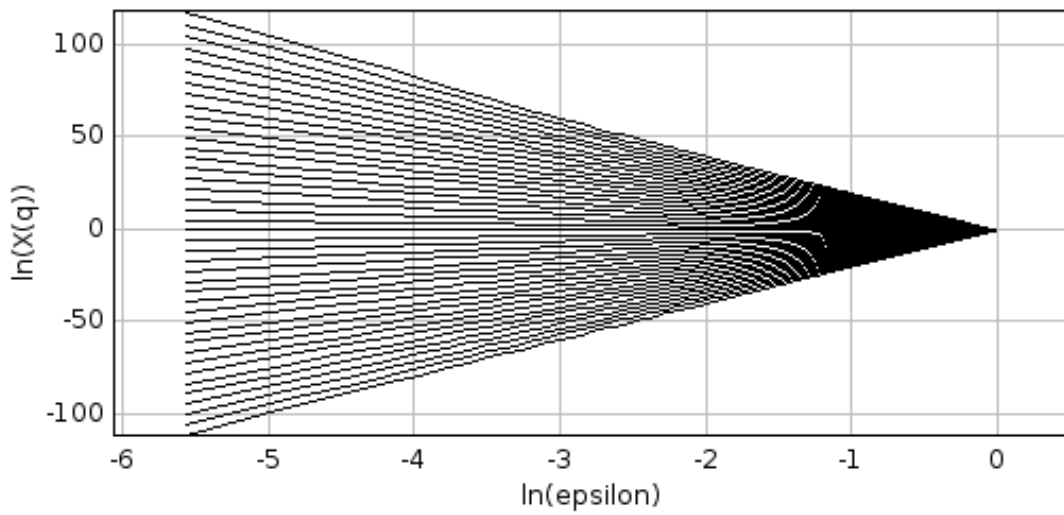


Figure A.4: $X(q, \epsilon)$ of the slice 128 from XY plane obtained through Gliding method

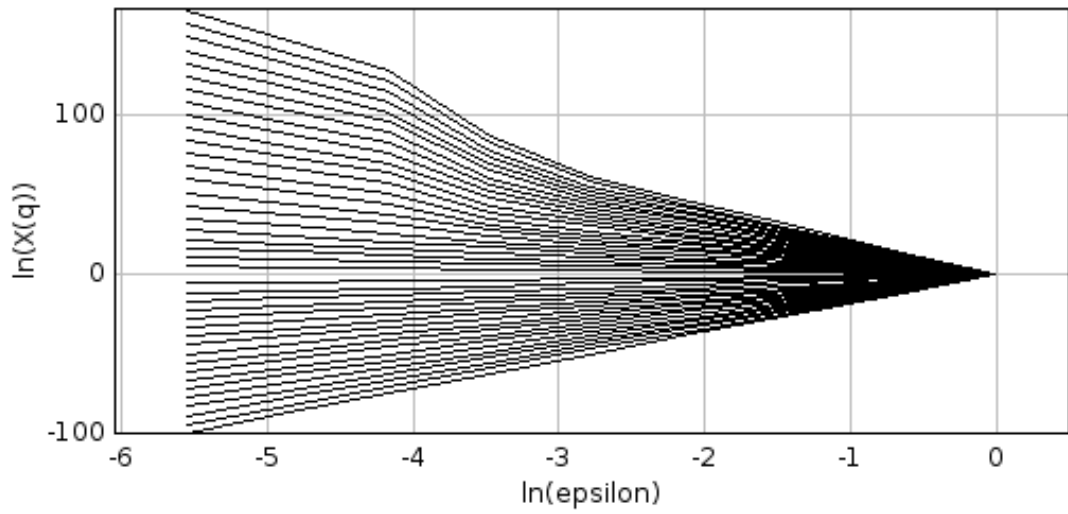


Figure A.5: $X(q, \epsilon)$ of the slice 192 from XY plane obtained through Box Counting method

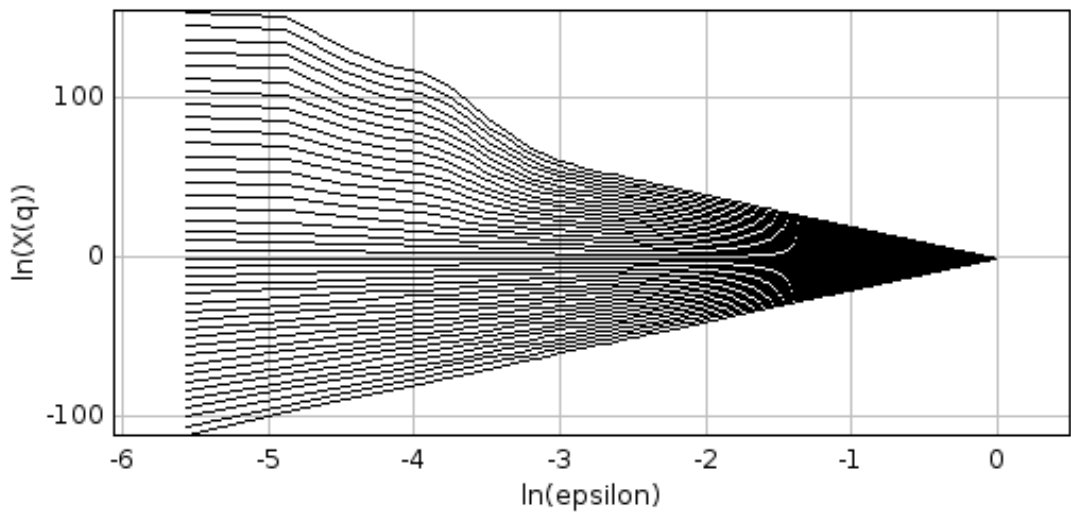


Figure A.6: $X(q, \epsilon)$ of the slice 192 from XY plane obtained through Gliding method

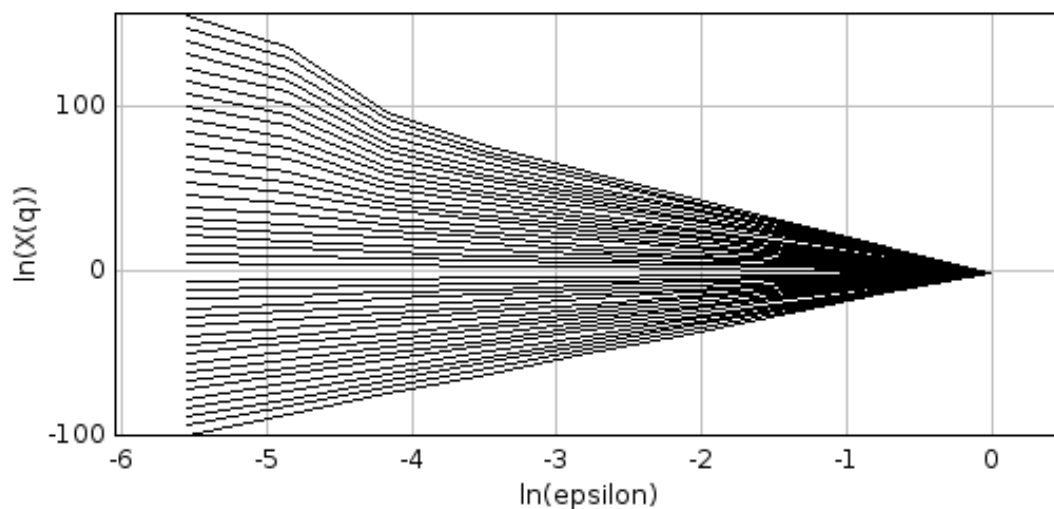


Figure A.7: $X(q, \epsilon)$ of the slice 64 from XZ plane obtained through Box Counting method

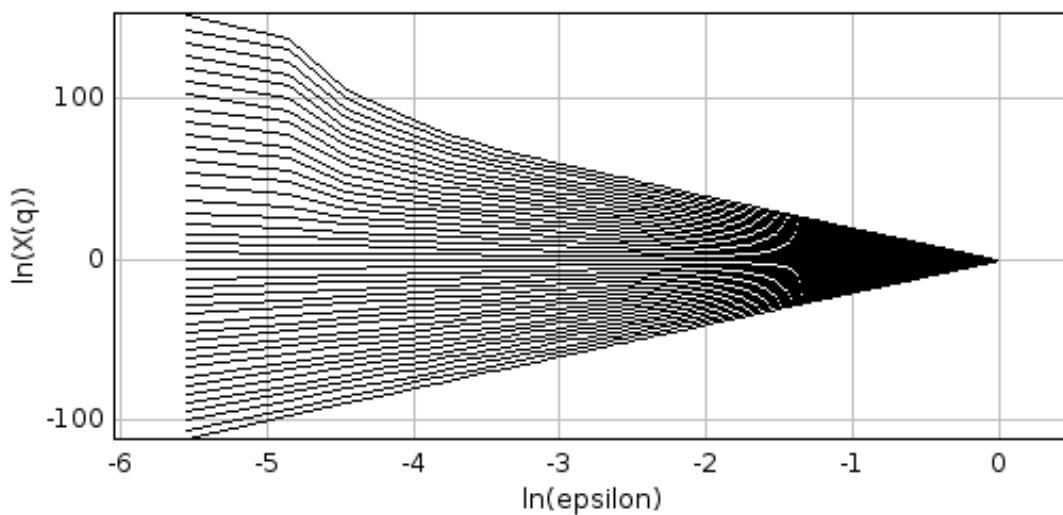


Figure A.8: $X(q, \epsilon)$ of the slice 64 from XZ plane obtained through Gliding method

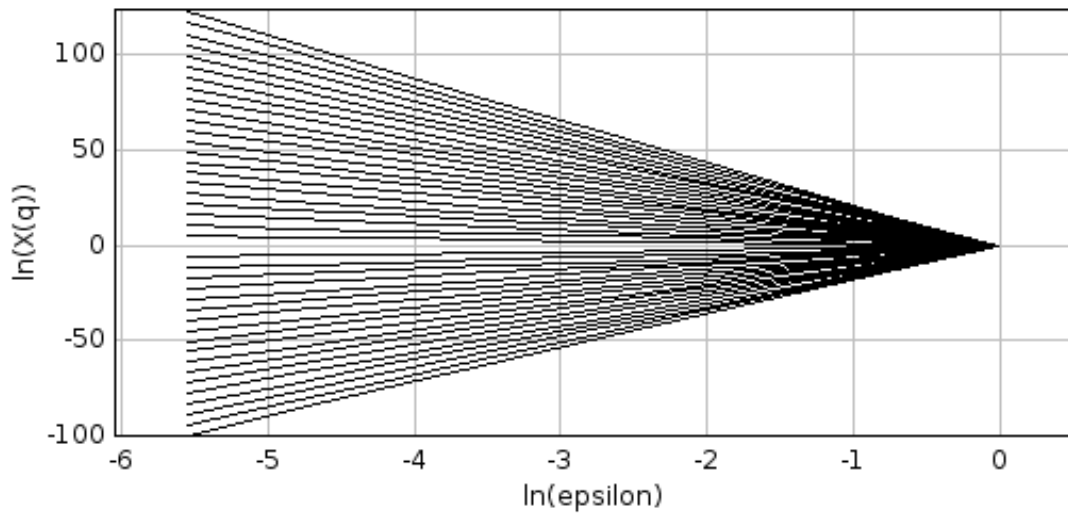


Figure A.9: $X(q, \epsilon)$ of the slice 128 from XZ plane obtained through Box Counting method

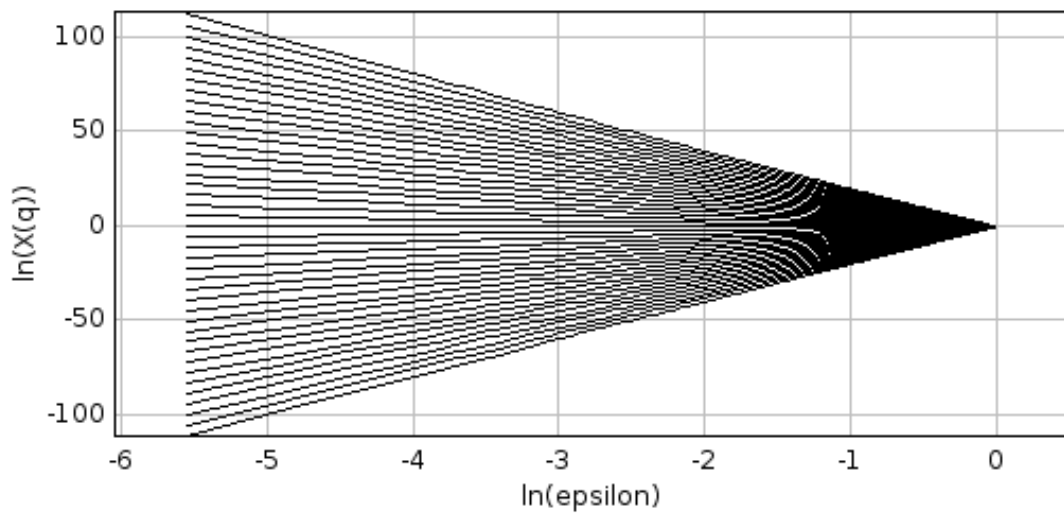


Figure A.10: $X(q, \epsilon)$ of the slice 128 from XZ plane obtained through Gliding method

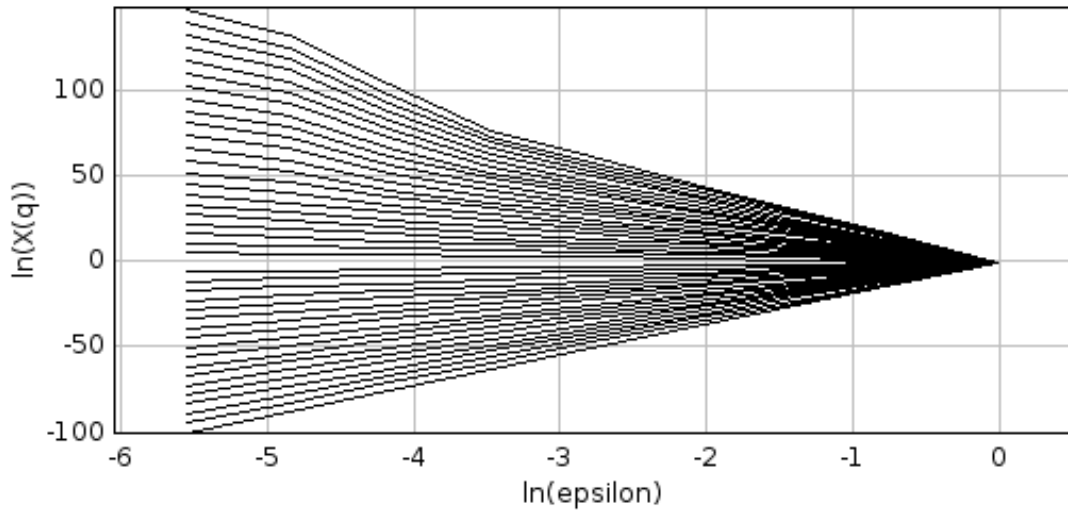


Figure A.11: $X(q, \epsilon)$ of the slice 192 from XZ plane obtained through Box Counting method

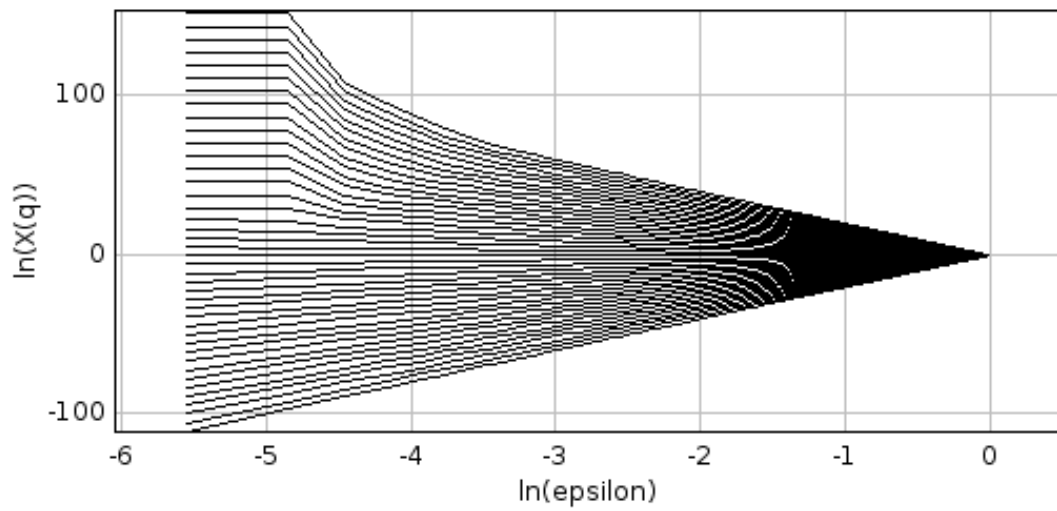


Figure A.12: $X(q, \epsilon)$ of the slice 192 from XZ plane obtained through Gliding method

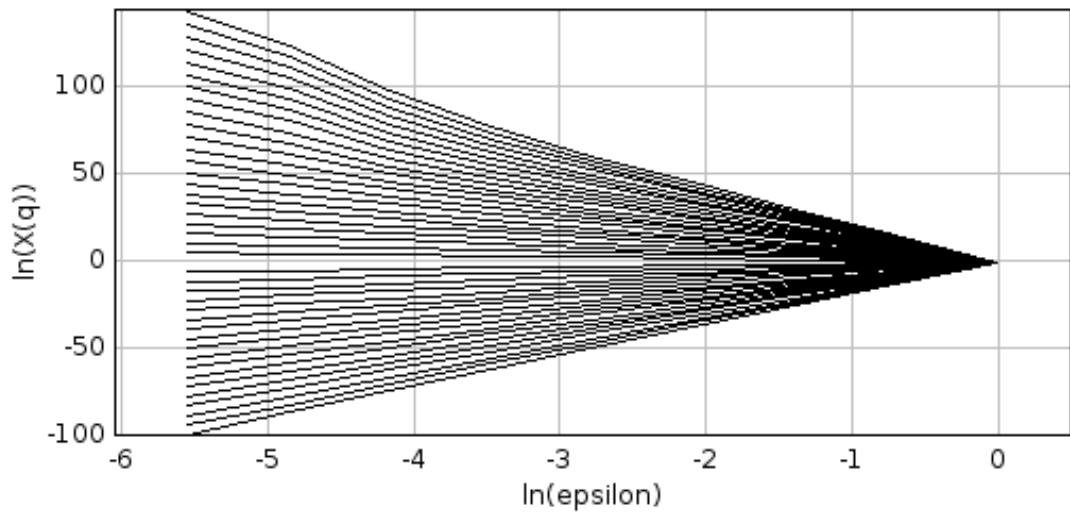


Figure A.13: $X(q, \epsilon)$ of the slice 64 from YZ plane obtained through Box Counting method

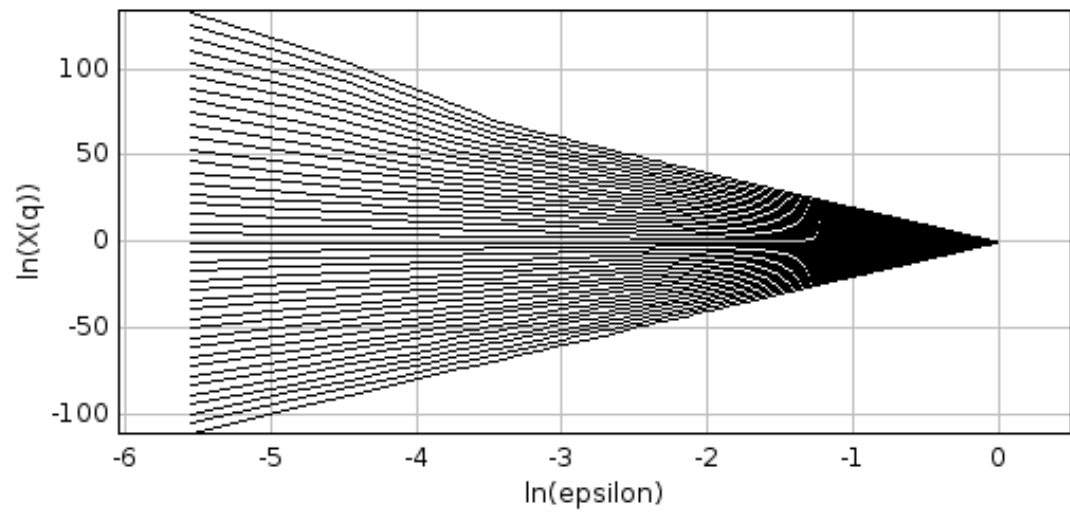


Figure A.14: $X(q, \epsilon)$ of the slice 64 from YZ plane obtained through Gliding method

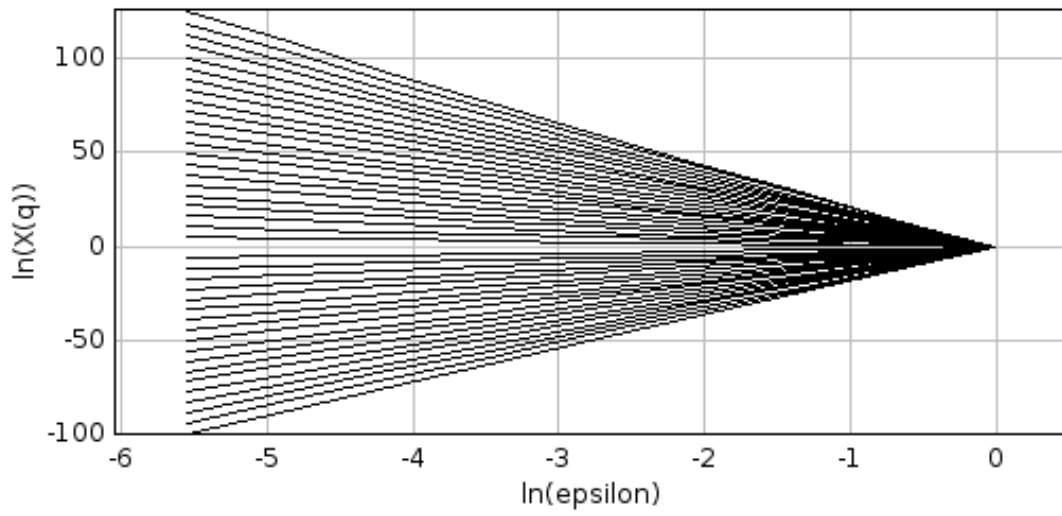


Figure A.15: $X(q, \epsilon)$ of the slice 128 from YZ plane obtained through Box Counting method

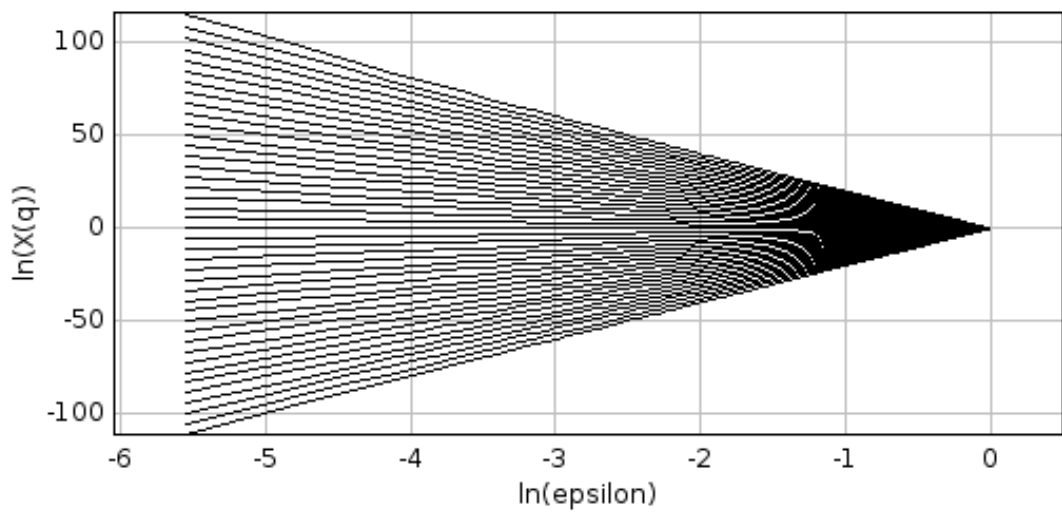


Figure A.16: $X(q, \epsilon)$ of the slice 128 from YZ plane obtained through Gliding method

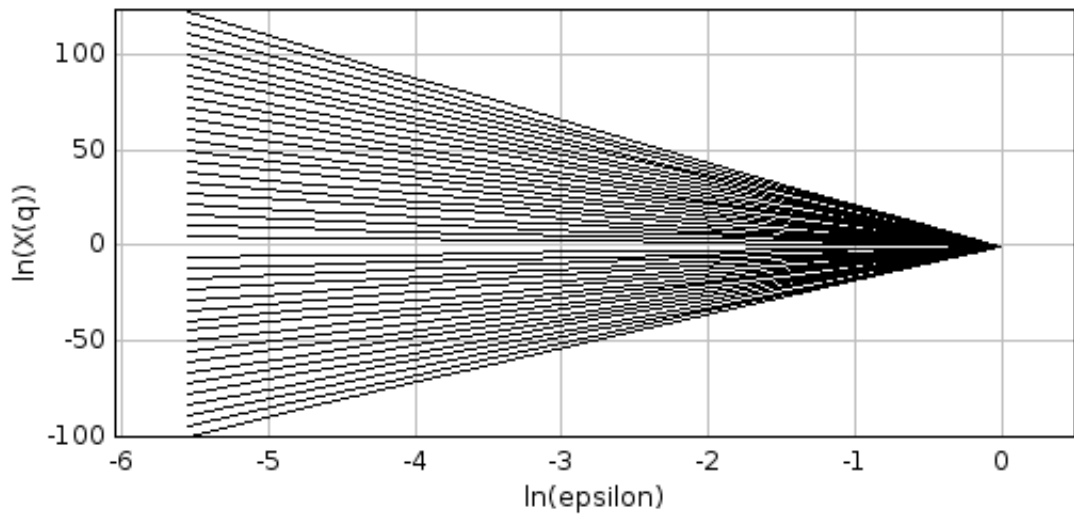


Figure A.17: $X(q, \epsilon)$ of the slice 192 from YZ plane obtained through Box Counting method

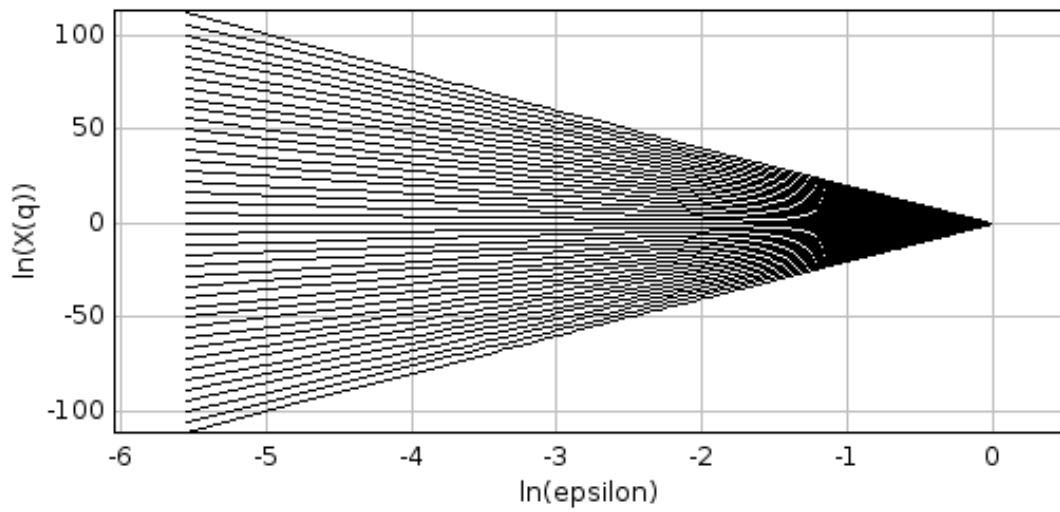


Figure A.18: $X(q, \epsilon)$ of the slice 192 from YZ plane obtained through Gliding method

Appendix B

$X(q, \epsilon)$ list of 3D soil aggregates
sample analysed with different
methods and sizes

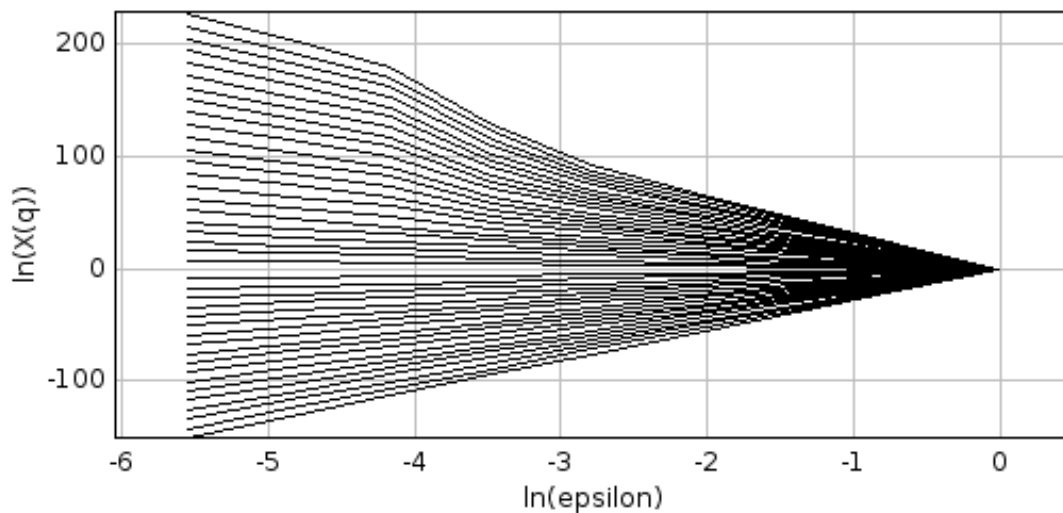


Figure B.1: $X(q, \epsilon)$ from the 256x256x256 voxel 3D model obtained through Box Counting method

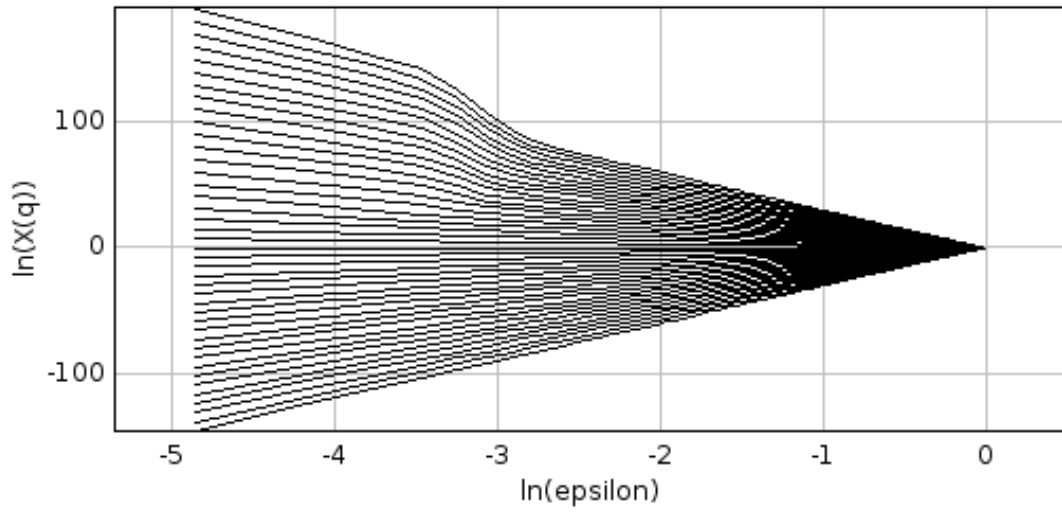


Figure B.2: $X(q, \epsilon)$ from the 128x128x128 voxel 3D model obtained through Gliding method

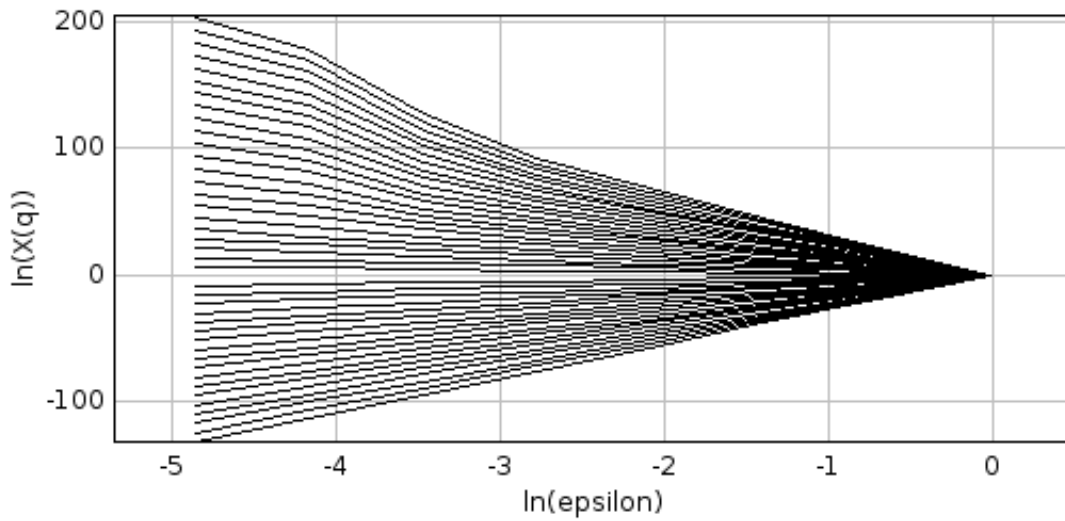


Figure B.3: $X(q, \epsilon)$ from the 128x128x128 voxel 3D model obtained through Box Counting method

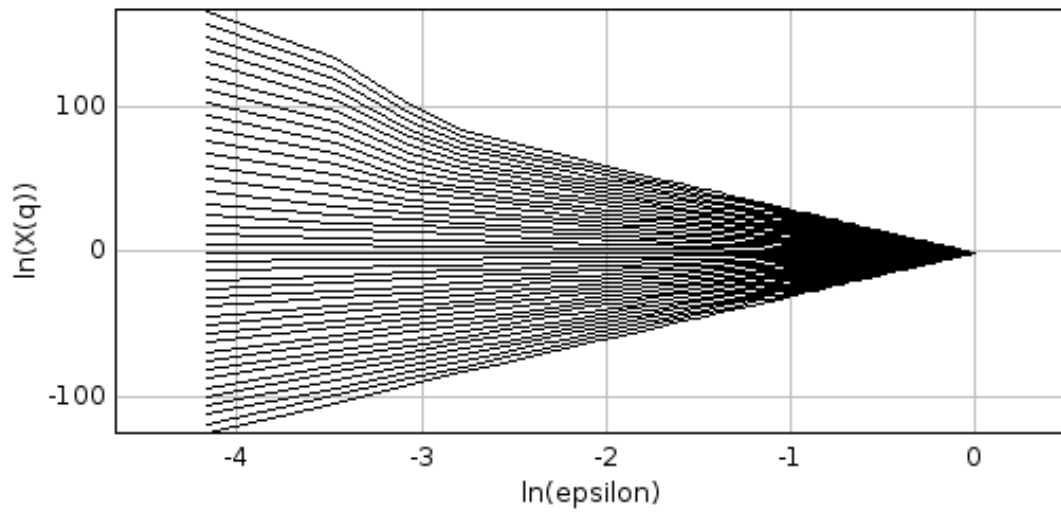


Figure B.4: $X(q, \epsilon)$ from the 64x64x64 voxel 3D model obtained through Gliding method

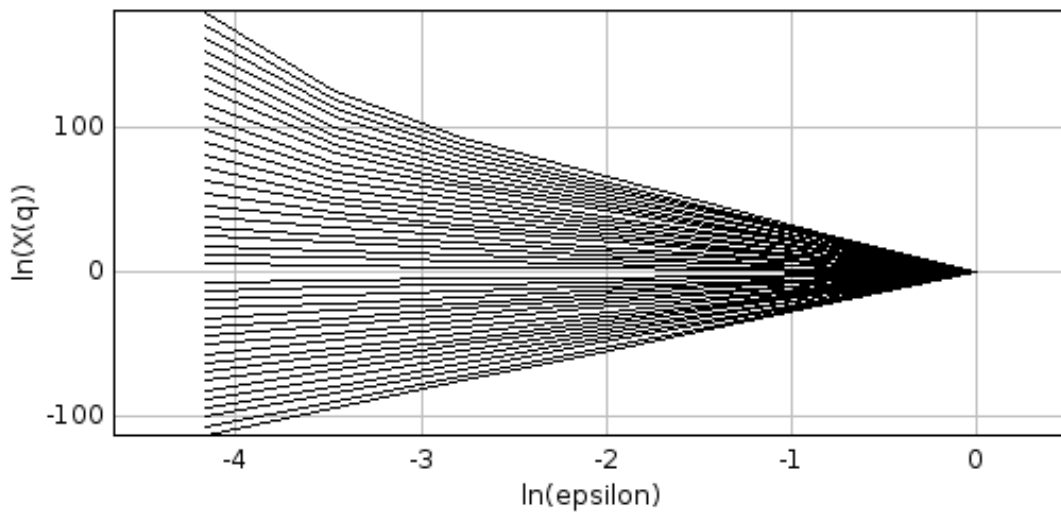


Figure B.5: $X(q, \epsilon)$ from the 64x64x64 voxel 3D model obtained through Box Counting method

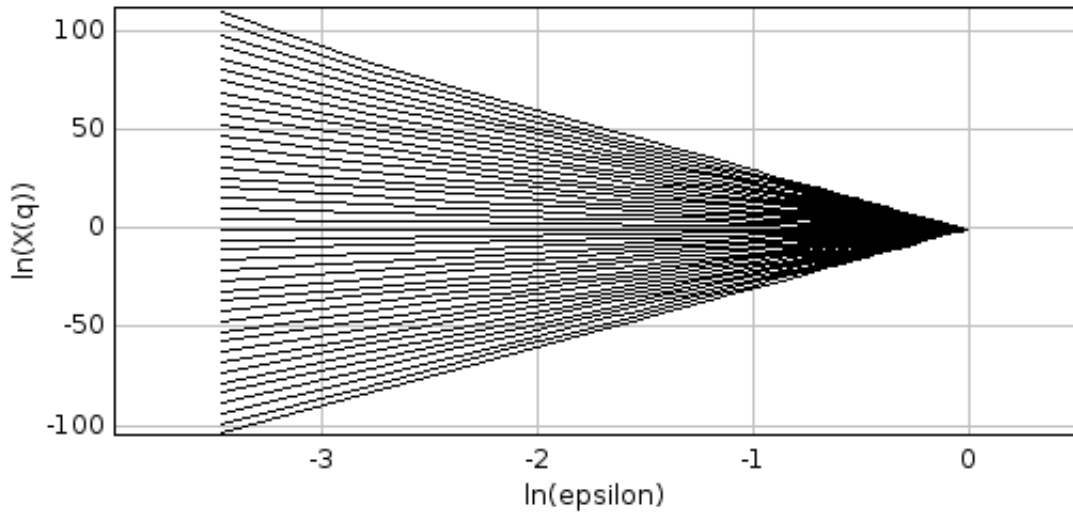


Figure B.6: $X(q, \epsilon)$ from the 32x32x32 voxel 3D model obtained through Gliding method

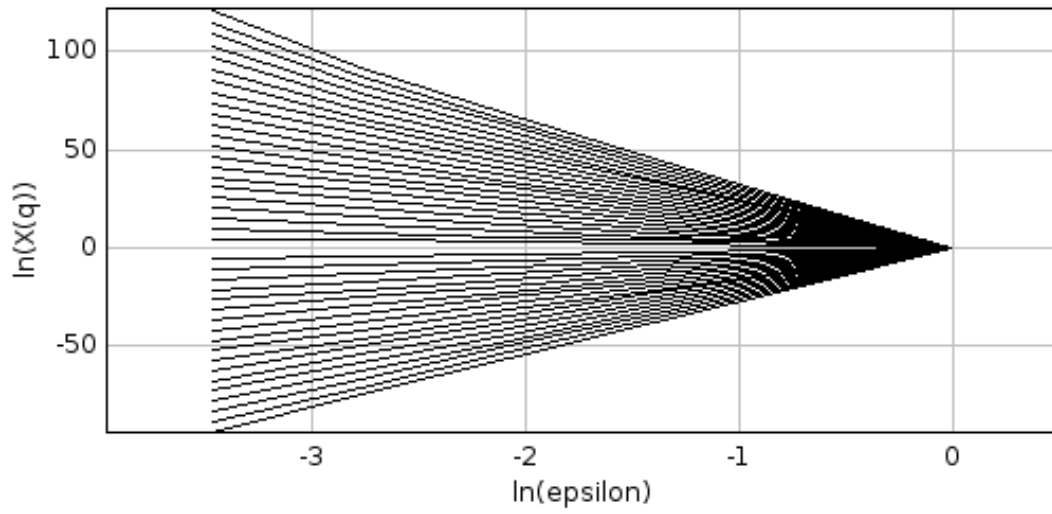


Figure B.7: $X(q, \epsilon)$ from the 32x32x32 voxel 3D model obtained through Box Counting method

Appendix C

$X(q, \epsilon)$ list of 3D tillage
treatments soil samples analysed

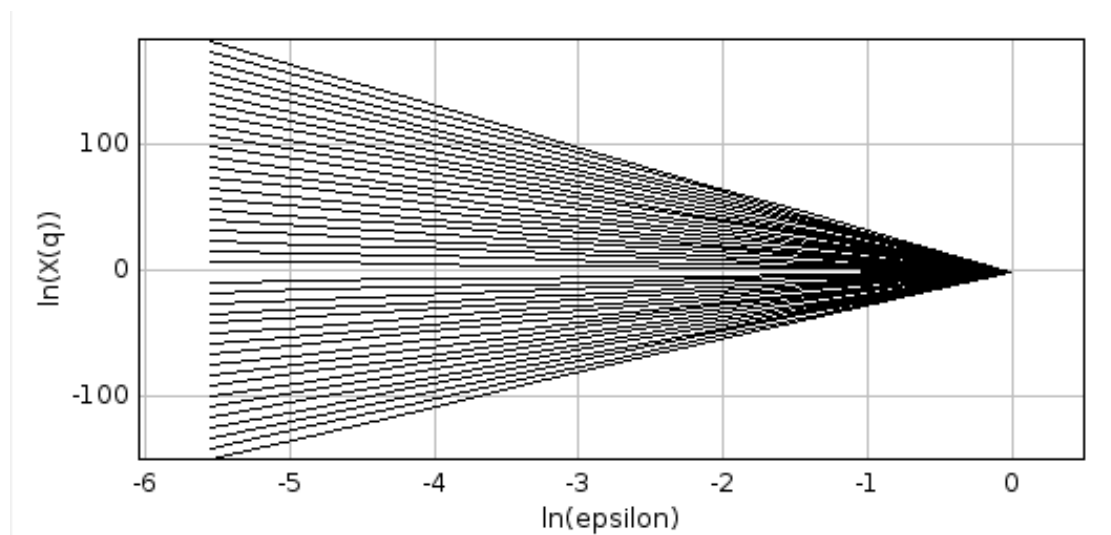


Figure C.1: $X(q, \epsilon)$ from the 256x256x256 voxel Vertedera 3D model obtained through Box Counting method

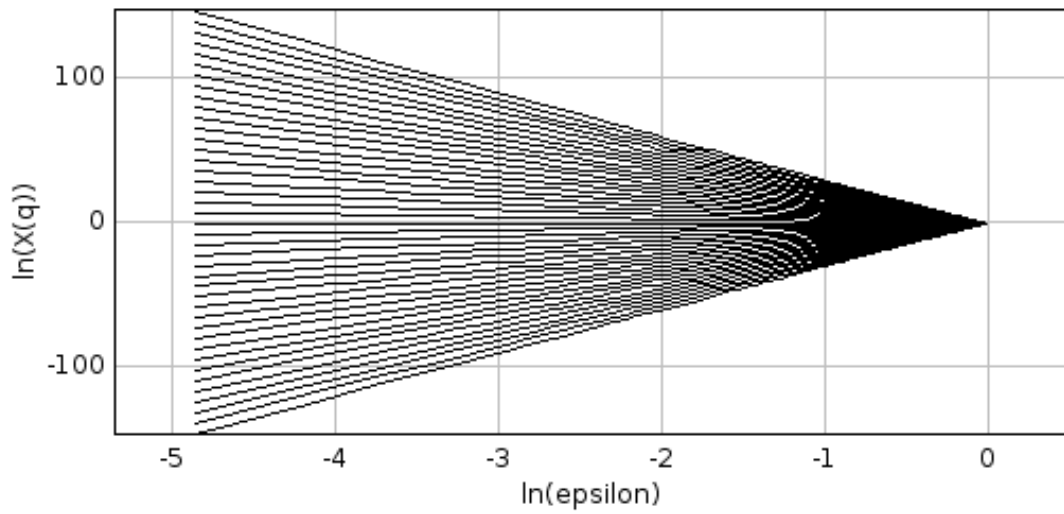


Figure C.2: $X(q, \epsilon)$ from the 128x128x128 voxel Vertedera 3D model obtained through Gliding method

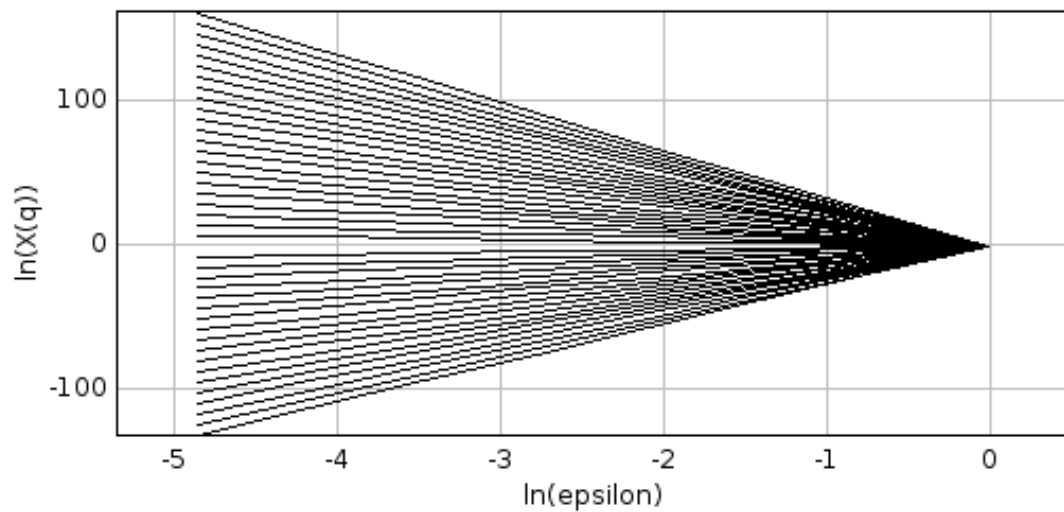


Figure C.3: $X(q, \epsilon)$ from the 128x128x128 voxel Vertedera 3D model obtained through Box Counting method

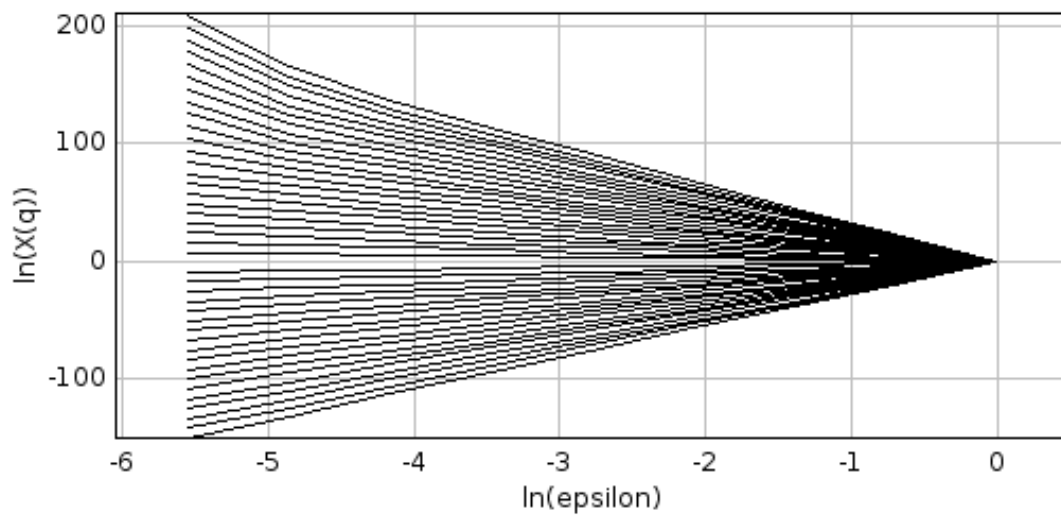


Figure C.4: $X(q, \epsilon)$ from the 256x256x256 voxel Chisell 3D model obtained through Box Counting method

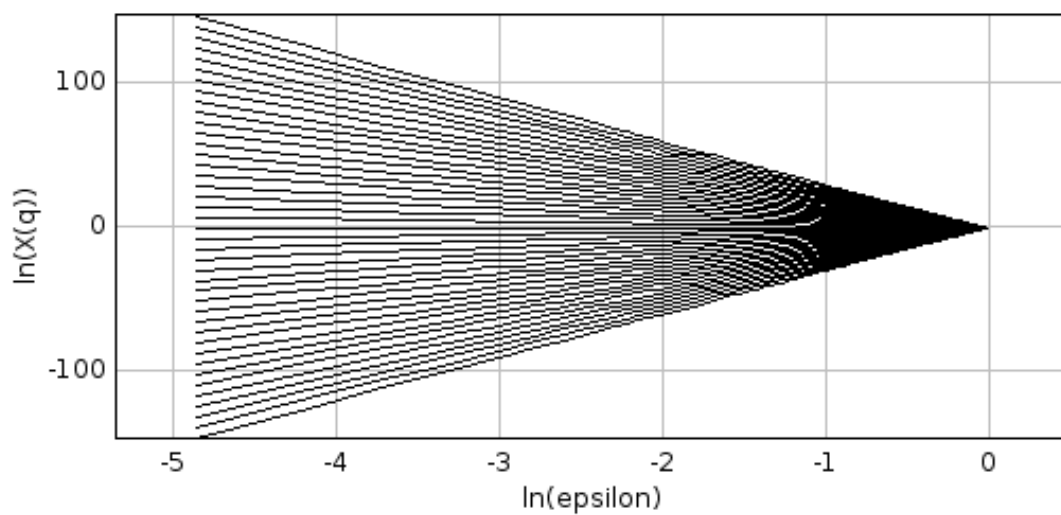


Figure C.5: $X(q, \epsilon)$ from the 128x128x128 voxel Vertedera 3D model obtained through Gliding method

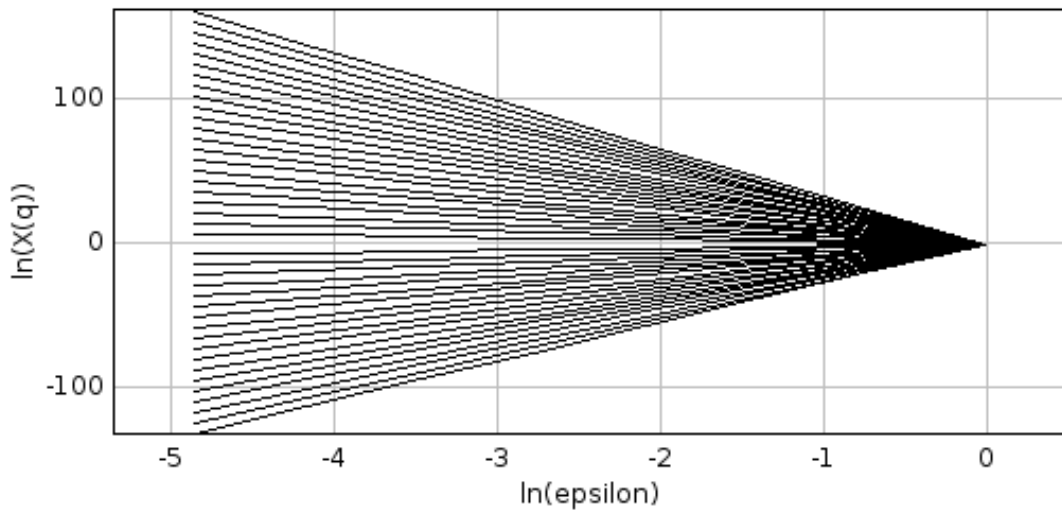


Figure C.6: $X(q, \epsilon)$ from the 128x128x128 voxel Chissel 3D model obtained through Box Counting method

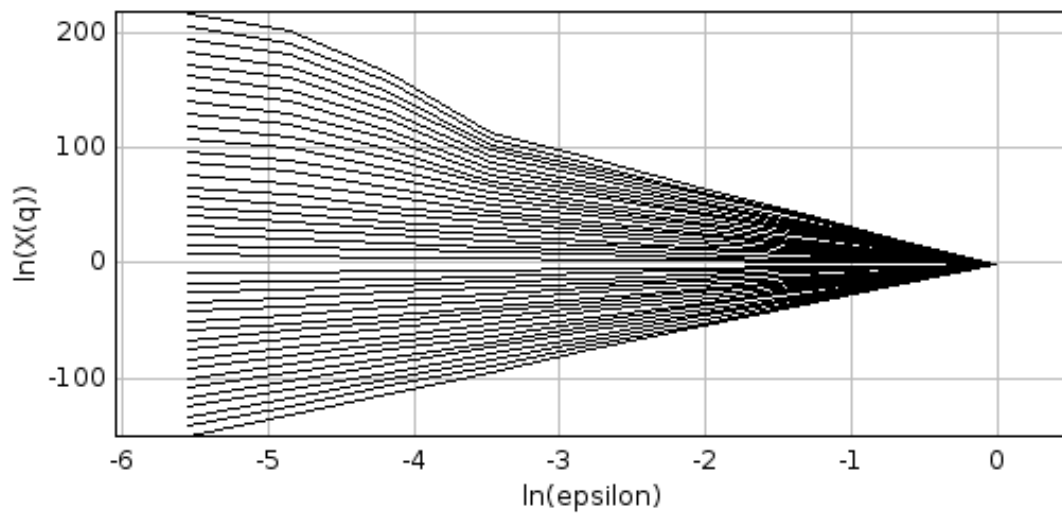


Figure C.7: $X(q, \epsilon)$ from the 256x256x256 voxel Roller 3D model obtained through Box Counting method

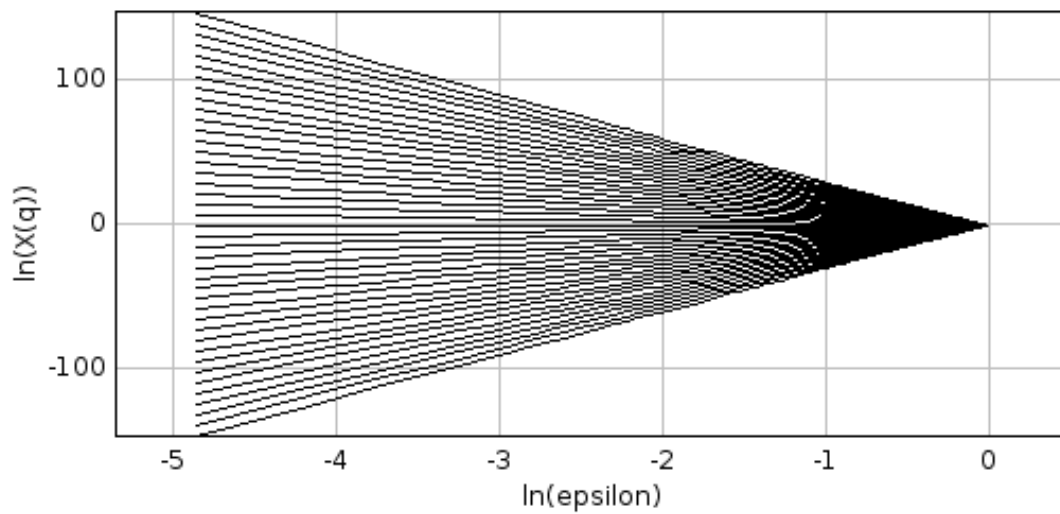


Figure C.8: $X(q, \epsilon)$ from the 128x128x128 voxel Vertedera 3D model obtained through Gliding method

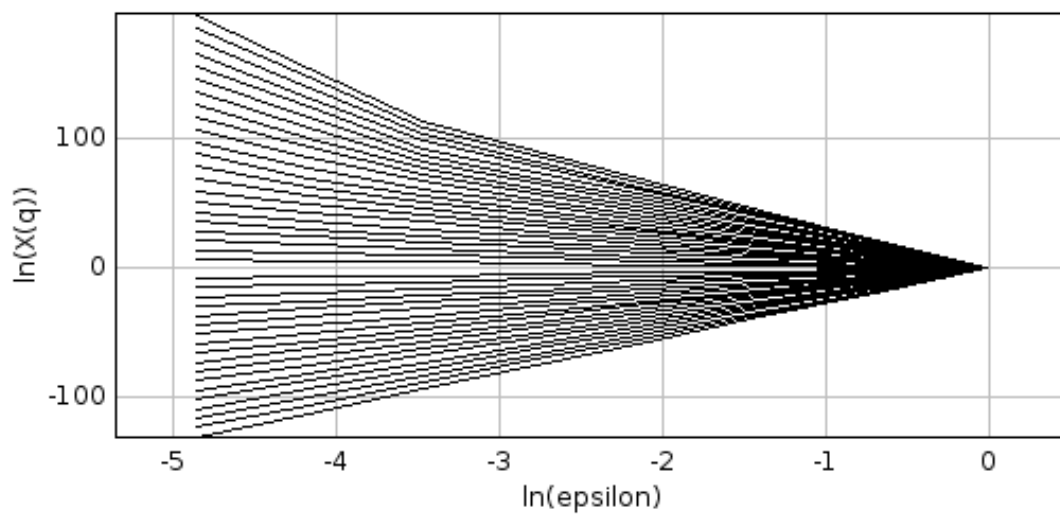


Figure C.9: $X(q, \epsilon)$ from the 128x128x128 voxel Roller 3D model obtained through Box Counting method

Appendix D

User manual and documentation
of the plug-in implemented in
ImageJ for multifractal analysis

User manual and documentation

Fractal analysis implemented in ImageJ

Iván G Torre¹, Richard J Heck², JC Losada¹, and Ana M Tarquis¹

¹Technical University of Madrid, Spain

²University of Guelph, Canada

June 16, 2014

Contents

1	Introduction	2
1.1	Structure and first steps	2
1.2	Internal structure	3
1.3	Some numerical details	4
1.3.1	Inverting images	4
1.3.2	Resize image	4
1.3.3	Calculation precision	5
2	Box Counting method	6
2.1	Monofractal analysis	6
2.1.1	Program: operation and results	6
2.1.2	Example 1: Sierpinsky carpet	8
2.2	Multifractal analysis	10
2.2.1	Program: operation and results	11
2.2.2	Example 2: Multifractal Sierpinski Carpet	13
3	Gliding Box method	17
3.1	Program: operation and results	17
3.2	Example 3: Landsat TM imagery	19
	References	23

1 Introduction

This document intends to be a basic user and an advanced programmers manual. It provides the formulas, algorithms and implementation methods that have been used in the plugin developed for ImageJ. This plugin analyse images through different multifractals methods.

ImageJ is a public domain Java image processing program. It runs, either as an online applet or as a downloadable application in Windows, Linux and Mac OS. ImageJ is optimized for processing 8-bit, 16-bit and 32-bit images. It supports standard stacks, a series of images that share a single window (3D images). It is multi-threaded, so time-consuming operations such as image file reading can be performed in parallel with other operations [1].

1.1 Structure and first steps

The plugin has implemented the Box Counting and the Gliding multifractal analysis in 2D and 3D images. For the Box Counting method it also perform monofractal analysis of Black and White images. Each method runs independent of others.

Before starting ImageJ, the folder which contains all Java methods must be copied to “plugin“ sub-folder in ImageJ installation directory. Then start ImageJ and open a 2D or stack image. Finally going to ”Plugin/Multifractal soil analysis“ choose a proper multifractal analysis of the ones developed in this plugin as seen in Figure 1.

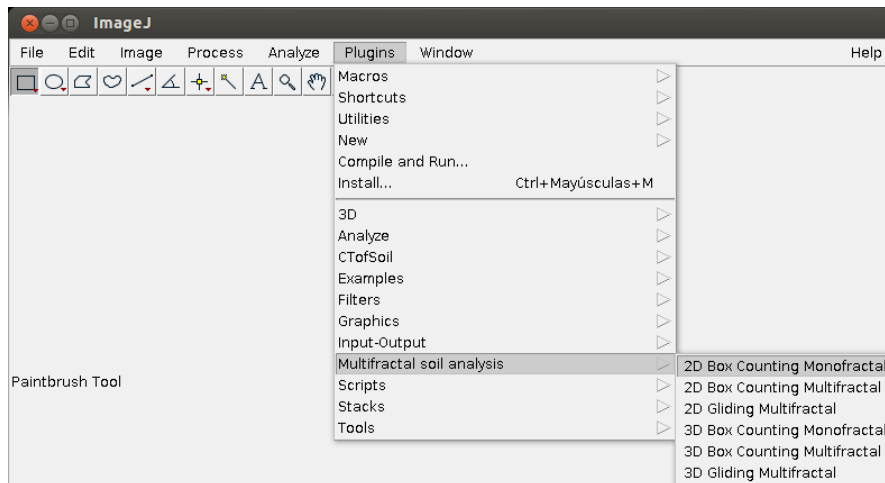


Figure 1: Different type of multifractal analysis from the plugin developed in ImageJ

1.2 Internal structure

The program is developed in Java using the methods implemented in ImageJ. Those methods are suitable and optimized for processing images. The plugin has been developed in a modular way and the internal structure is shown schematically in Figure 2.

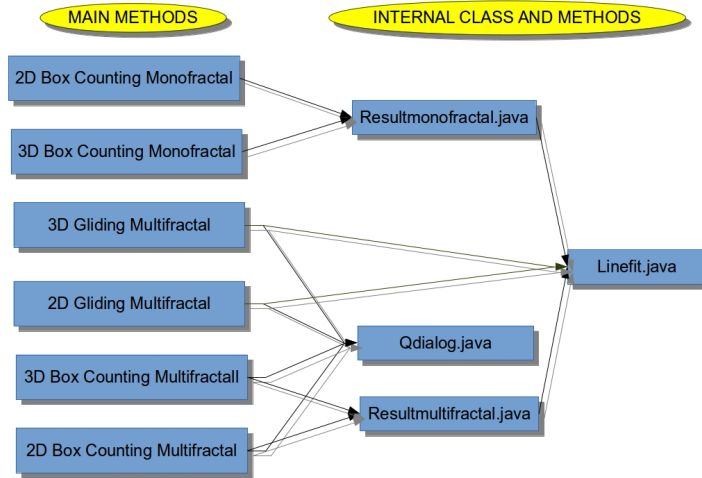


Figure 2: Internal structure of the Java class and methods developed for the plugin

1.3 Some numerical details

1.3.1 Inverting images

Although the program can be applied to any type of image, it is meant for calculating the pore structure of soils. So when it does a fractal or multifractal analysis it gives the more importance to the dark holes of the image which means to be the pores. The algorithm of the method is based on the density of the pixels, but a black hole has value of 0 while a white pixel has the maximum value (255 in case of 8-bit images for example). So for applying the algorithm correctly the image is inverted before the calculations and then again re-inverted for showing the original image. For inverting the image the program will do the next operation:

$$pixel_{inverted} = |(2^{bit} - 1) - original_{pixel}| \quad (1)$$

Where bit refers to the depth of the image (8-bit, 16-bit...)

1.3.2 Resize image

In Box Counting Method sometimes the user can select to resize the image to a properly size (see below). The algorithm implemented for doing this is bilinear

interpolation. The key idea is to perform linear interpolation first in one direction, and then again in the other direction. Although each step is linear in the sampled values and in the position, the interpolation as a whole is not linear but rather quadratic in the sample location. Bilinear interpolation considers the closest 2x2 neighbourhood of known pixel values surrounding the unknown pixel's computed location. It then takes a weighted average of these 4 pixels to arrive at its final, interpolated value. The weight on each of the 4 pixel values is based on the computed pixel's distance (in 2D space) from each of the known points.

1.3.3 Calculation precision

All the calculates done in the program uses double precision. Although sometimes it only shows 4 or 5 decimals, it will always retain all the decimals.

Double-precision floating-point format is a computer number format that occupies 8 bytes (64 bits) in computer memory and represents a wide dynamic range of values by using floating point. This gives from 15–17 significant decimal digits precision.

2 Box Counting method

Box counting is a method of gathering data for analysing complex patterns by breaking an image into a smaller and smaller pieces. The intend of box counting is to quantify fractal scaling. In the algorithm implemented the boxes are scaled in power of two sizes on. Therefore it is necessary for processing the image that its size in pixels is a power of 2. So, if the user does not have its image in the properly size the program will ask her to cut or resize it.

2.1 Monofractal analysis

Fractal dimension is the most important parameter of monofractal theory. In box counting method it counts the number of square grids required to entirely cover an object surface. Let ϵ be the adimensional side length of the grid (size length of the grid divided by total size length) , $N(\epsilon)$ be the number of grids required to cover the black area in the image for each size. The fractal dimension of an image can be defined as the relationship between the number of grids and the its size with the next expression [2]:

$$D = \lim_{\epsilon \rightarrow 0} \frac{\log N(\epsilon)}{\log \frac{1}{\epsilon}} \quad (2)$$

so the fractal dimension D, can be estimated numerically as the slope of the line:

$$\log N = D \log \frac{1}{\epsilon} + cte \quad (3)$$

2.1.1 Program: operation and results

The method works also with Black and White and Gray 2D images or 3D images saved as stacks. So after opening the file go to sub-menu "plugin/Multifractal soil analysis/2D Box Counting Monofractal" for 2D images or "plugin/Multifractal soil analysis/3D Box Counting Monofractal" for 3D images. If the image size in pixels of the image is not a power of 2, then it will appear a dialogue asking to resize or cut the image (Figure 3). The image will be reduced to the largest size power of 2 smaller than itself.

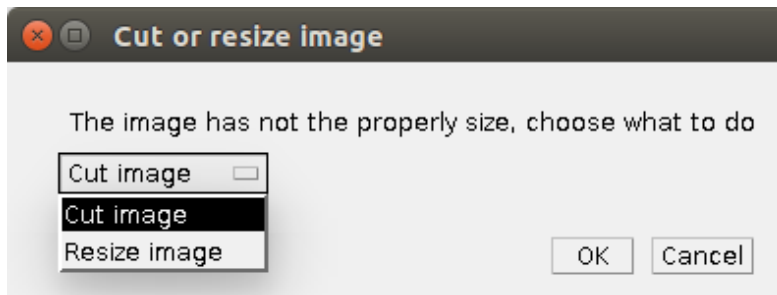


Figure 3: Cut or resize the image

After scaling the image, if the image is not in black and white colours it will be automatic converted. Then will appear a dialogue (Figure 4) where the user can choose to analyze the actual image or the inversed one.

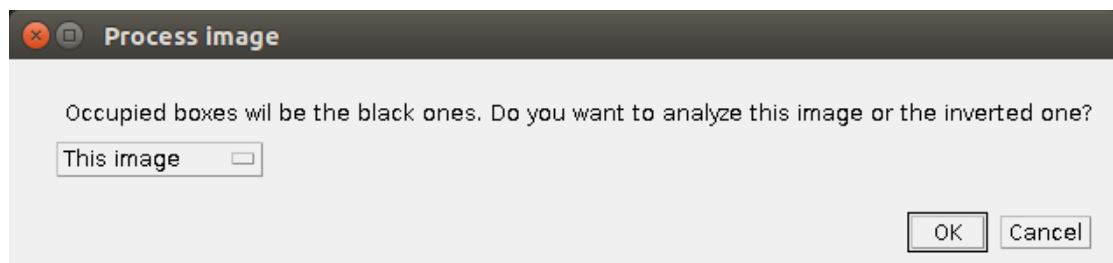


Figure 4: Choose between the actual image or the inverted one

Then the user can select the minimum and maximum size of the boxes (in pixels) that will be used along analysis. In Figure 5 the numbers shows are the limits that can be choosen. If the value that introduces the user is not power of 2, then it will be rounded.

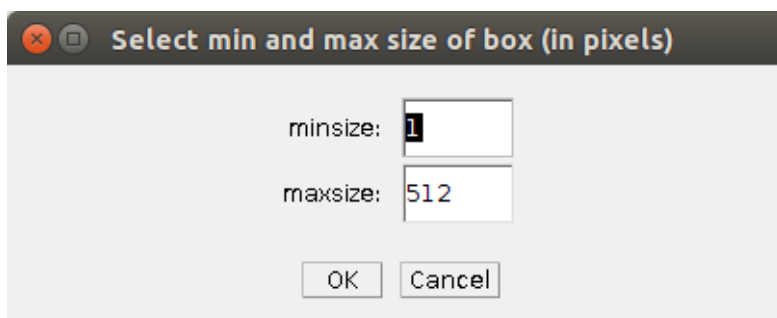


Figure 5: Choose the maximum and minimum size of the boxes for the analysis

Now the program realizes the box counting calculations and finally shows the results. In the next section the method is validated calculating the fractal dimension of the sierpinsky carpet.

2.1.2 Example 1: Sierpinsky carpet

In this example we are going to evaluate the method calculating the fractal dimension of the Sierpinsky carpet(Figure 6).

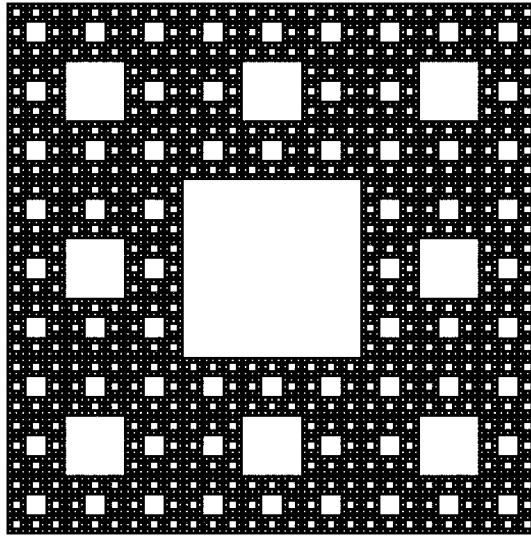


Figure 6: Sierpinsky Carpet

For this example we have resize the image and used all rage of box sizes possible for the sample.

After realizing the calculations, the Figure 7 shows for each adimensional size of the box ϵ , the total number of boxes and the number of boxes with at least one black pixel.

Results for 2D Monofractal Box Counting method			
	epsilon	Total boxes	Occupied boxes
1	1.000	1.000	1.000
2	0.500	4.000	4.000
3	0.250	16.000	16.000
4	0.125	64.000	60.000
5	0.062	256.000	240.000
6	0.031	1024.000	892.000
7	0.016	4096.000	3084.000
8	0.008	16384.000	10952.000
9	0.004	65536.000	39924.000
10	0.002	262144.000	144823.000

Figure 7: For each adimensional size ϵ of the box counting method, total number of boxes, and number of boxes with at least one black pixel.

The program also plots the the results in a new window. In Figure 8 compares in log-log the number of boxes with at least one black pixel as a function of the size ϵ . It realizes the linear fit of the points showing its parameters and the goodness of the fit R^2 . The slope of the line will be the fractal dimension of the picture.

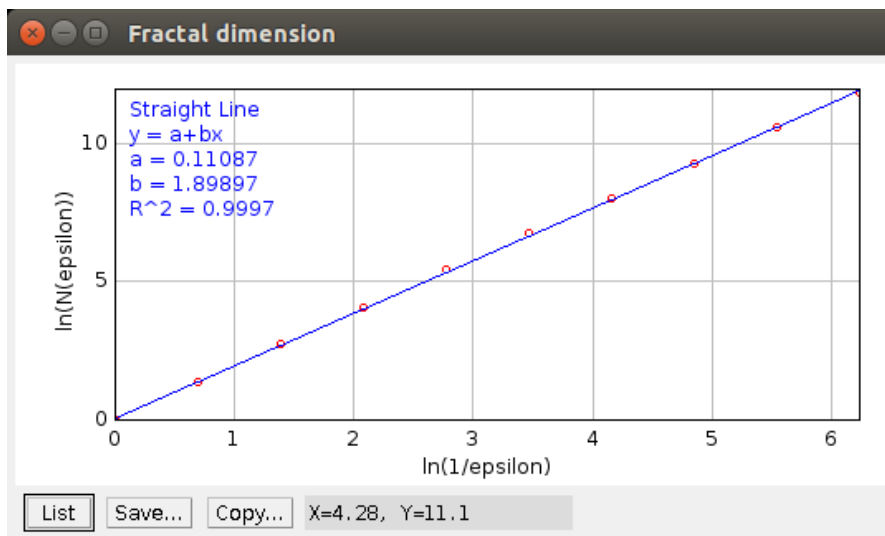


Figure 8: Comparison in log-log between the number of boxes with at least one black pixel and the size ϵ

Pushing the widow 'List', the two first columns (X0,Y0) are the values used for

plotting the linear regression, and the two second columns (X1,Y1) are the values obtained from the analyzed image.

Finally the last figure (Figure 9) shows the fractal dimension of the picture we have analysed with the error of the linear fit of the slope. It shows the goodness of the calculations because the calculated fractal dimension is 1.898 versus 1.892 which is the theoretical fractal dimension of the sierpinsky carpet.

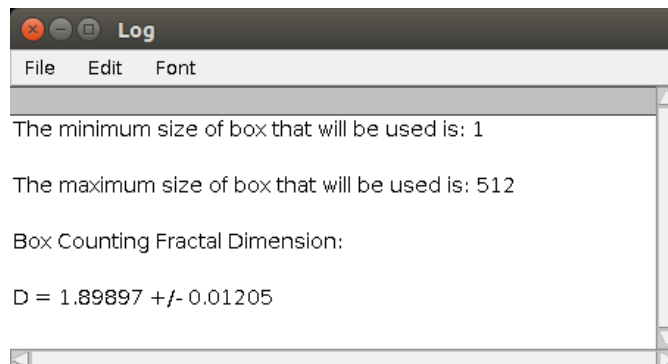


Figure 9: Fractal dimension of the picture

2.2 Multifractal analysis

A multifractal system is a generalization of the fractal analysis in which a single exponent, the fractal dimension, is not enough to describe its dynamics; instead, a continuous spectrum of exponents is needed. In essence, multifractal analysis applies a distorting factor to datasets extracted from patterns, to compare how the data behave at each distortion sometimes giving more or less importance to the high or low mass density areas of the picture. This is done using graphs known as multifractal spectra that illustrate how the distortions affect the data.

So if we cover the picture with boxes of size ϵ and define $P_i(\epsilon)$ as the probability of this mass at i relative to the total mass of the picture for a box size ϵ , then the generalized dimensions D_q which corresponds to scaling exponents for the q th moments of the measure are defined as [3]:

$$D_q = \frac{1}{q-1} \lim_{\epsilon \rightarrow 0} \frac{\log \sum_i P_i^q(\epsilon)}{\log \epsilon} = \frac{1}{q-1} \lim_{\epsilon \rightarrow 0} \frac{\log X(\epsilon)}{\log \epsilon} \quad (4)$$

for $q \neq 1$. For $q = 1$, D_1 is defined by taking the limit when q approaches 1 and by using L'Hopital's Rule [4]:

$$D_1 = \lim_{\epsilon \rightarrow 0} \frac{\sum_i P_i(\epsilon) \log P_i(\epsilon)}{\log \epsilon} \quad (5)$$

This measure is correlated with the mass exponent $\tau(q)$ as follows:

$$\tau_q = (q - 1)D_q \quad (6)$$

for $q \neq 1$ and $\tau(1) = 0$.

Another interesting measure in multifractal analysis is the relationship between a Hausdorff dimension f and an average singularity strength α as implicit functions of the parameter q . Those are defined as follows:

$$f(\alpha) = q\alpha - \tau \quad (7)$$

$$\alpha = \frac{d\tau}{dq} \quad (8)$$

An easily used definition of the singularity spectrum which is the one that have been implemented in this ImageJ plugin is:

$$f(q) = \lim_{\epsilon \rightarrow 0} \frac{\sum_i \mu_i(q, \epsilon) \log \mu_i(q, \epsilon)}{\log L} \quad (9)$$

$$\alpha(q) = \lim_{\epsilon \rightarrow 0} \frac{\sum_i \mu_i(q, \epsilon) \log P_i(q, \epsilon)}{\log L} \quad (10)$$

where $\mu_i(q, \epsilon)$ is how the distorted mass probability at a box compares to the distorted sum over all boxes at this box size:

$$\mu_i(q, \epsilon) = \frac{(P_j(\epsilon))^q}{\sum_j (P_j(\epsilon))^q} \quad (11)$$

2.2.1 Program: operation and results

This module is also implemented for 3D and 2D images. First the user has to open the image (or stack image in 3D) and then click the module in "plugin/Multifractal soil analysis/2D Box Counting Multifractal" for 2D images or "plugin/Multifractal soil analysis/3D Box Counting Multifractal" for 3D images. After that will be appear a box where the user will define the range of the multifractal exponents q , giving its minimum, maximum value and the interval.(Figure 10)

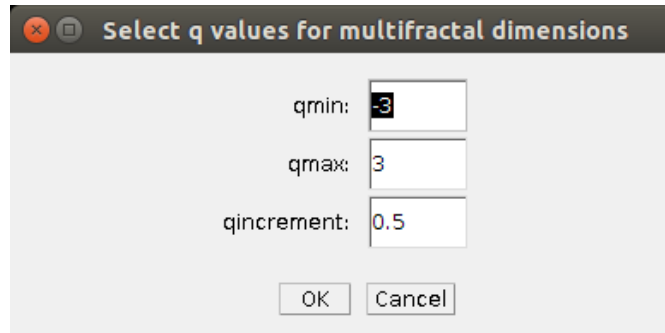


Figure 10: Dialogue about q exponents

Then, if the image size in pixels is not a power of 2, then it will appear a dialogue asking to resize or cut the image (Figure 11). The image will be reduced to the largest size power of 2 smaller than itself.

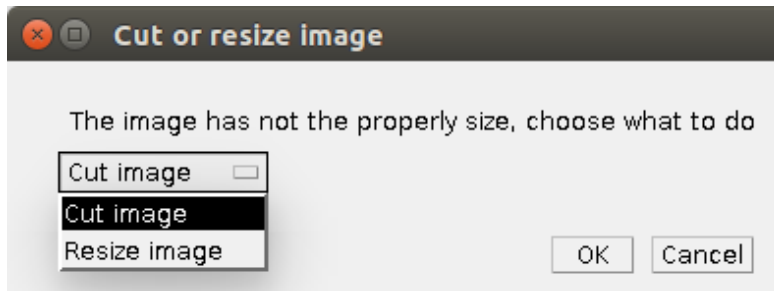


Figure 11: Cut or resize the image

Then will appear a dialogue (Figure 12) where the user can choose to analyze the actual image or the inversed one.

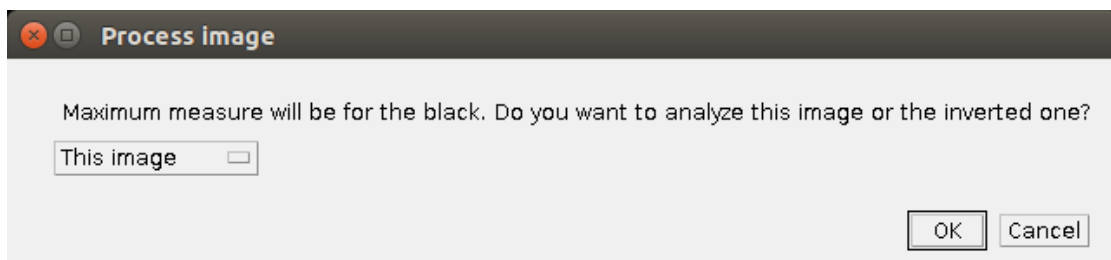


Figure 12: Choose between the actual image or the inversed one

Then the user can select the minimum size of the boxes (in pixels) that will

be used along analysis. In Figure 13 the numbers shows are the limits that can be chosen. If the value that introduces the user is not power of 2, then it will be rounded.

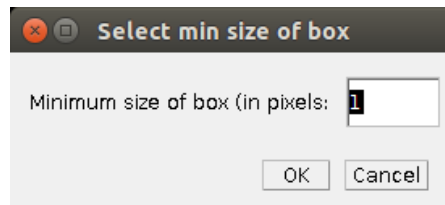


Figure 13: Choose the minimum size of the boxes for the analysis

Finally the program realizes the multifractal box counting analysis and shows the results. The plots and the tables that are shown by the program are fully explained with one example in the next section of this manual.

2.2.2 Example 2: Multifractal Sierpinski Carpet

Now we are going to applicant the method to a real example. For this porpouse we are going to analyse a multifractal sierpinski carpet in Gray colour. The Sierpinski carpet is generated with a probabilist method explained in [5] with a $p = 8/9$ and 5 iterations (Figure 14). We have resize the image, used all rage of box sizes possible for the sample and a range of q from -20 to 20.

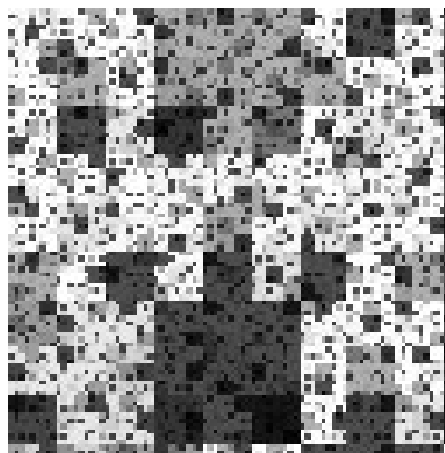


Figure 14: Multifractal Sierpinski Carpet with $p = 8/9$ and five iterations

After realizing the calculations the programme will show plots with the results. The Figure 15 shows $X(\epsilon)$ for each value of q . This will be used for calculating the slope and then get the Dq and more coefficients. We can run again the program and choose another value for epsilon max for getting a proper and uniformly slope.

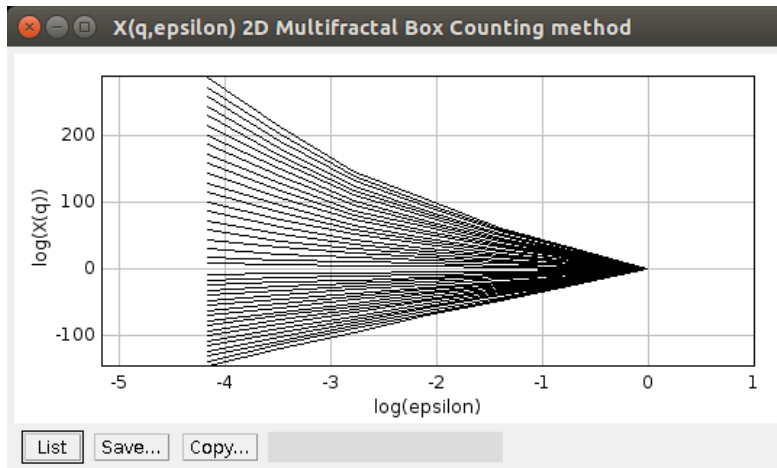


Figure 15: $X(q)$ vs ϵ

Pushing 'List' it shows the numeric values of the plot.

Then the programme get the slope τ of each line and plot versus the q values. (see Figure 16)

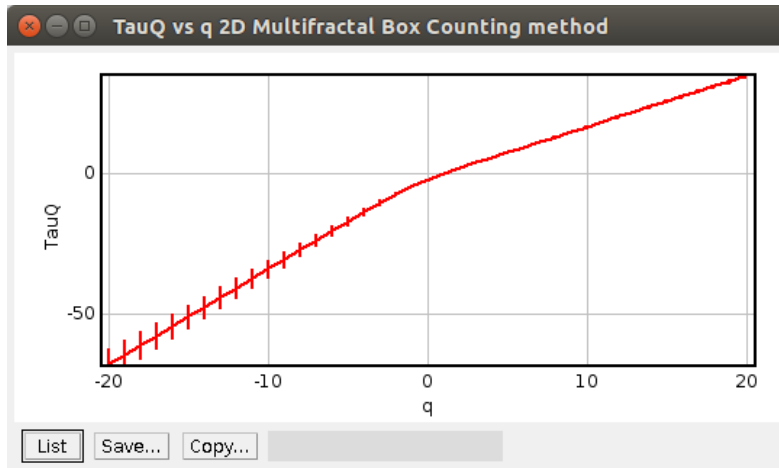


Figure 16: $\tau(q)$ vs q . The vertical lines shows the error associated with the calculation of τ

Pushing 'List' it shows the numeric values of the plot which it errors.

Then we get the values of Dq vs q associated to the analysed image (Figure 17). This shows the goodness of the method because the values are similar to the ones in [5]. The theoretical results are $Dq_{q \rightarrow -\infty} = 2.96$ and $Dq_{q \rightarrow +\infty} = 1.87$, very similar to the ones we have obtained given that the size of the image is limited and with only five iterations. The error bars in q negative are typically from the box counting method, because of the lack of statistic in areas with low density.

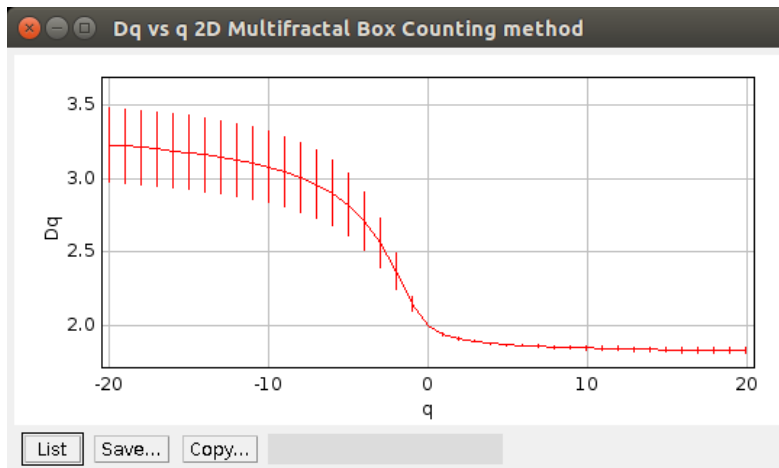


Figure 17: Dq vs q . The vertical lines shows the error associated with the measure

Pushing 'List' it shows the numeric values of the plot which it errors.

Finally it shows the plot of the multifractal spectrum (ordinate axis) versus its singularity strength α (abscissa axis). Horizontal and vertical bars are the multifractal spectrum and singularity strength errors

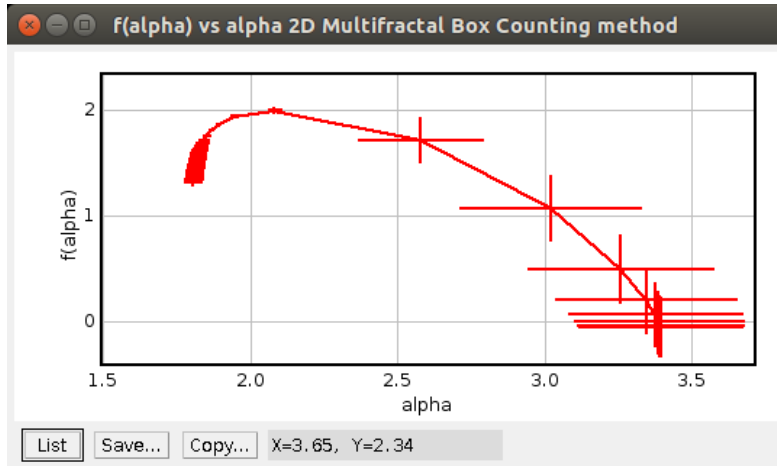


Figure 18: α vs $f(\alpha)$. The vertical and horizontal lines shows the error associated with the measure

Here the numeric values are not shown in 'List' button. The α and $f(\alpha)$ values with their errors for each q are shown in the table that the program shows.

3 Gliding Box method

Although the algorithm of the box counting method is very fast, it has the problem that for negative values of q the error of measures are very high. The gliding method will improve this area.

The gliding box method was originally used in lacunarity analysis and later modified by Cheng [6] for application to multifractal analysis and then used in soil analysis [7]. This method constructs samples by gliding a box of certain adimensional size ϵ over the grid map in all possible directions. An up-scaling partitioning process begins with a minimum line size smaller than 1. This method first estimates the mass exponent function $\tau(q)$:

$$\tau(q) + D = \lim_{\epsilon \rightarrow 0} \frac{\log\left(\frac{1}{N^*(\epsilon)} \sum_{i=1}^{N^*(\epsilon)} \mu_i^q(\epsilon)\right)}{\log \epsilon} \quad (12)$$

where ϵ is the adimensional box size, $N^*(\epsilon)$ represents total number of gliding boxes of that size and measure $\mu(\epsilon) \neq 0$ and D is the topological dimension of the object analysed ($D = 2$ for bi-dimensional objects and $D = 3$ for three-dimensional objects)

The functions α and $f(\alpha)$ are estimated numerically by the Legendre transformation as

$$\alpha(q) = \frac{d\tau(q)}{dq}, \quad f(\alpha) = \alpha(q)q - \tau(q) \quad (13)$$

One advantage of gliding box method is that the larger sample size it provides usually yields better statistical results. The disadvantage is that needs more calculation time because of the great number of operations.

3.1 Program: operation and results

Operation of this module is quite similar to the previous ones, even simpler. It is implemented for 3D and 2D images. First the user has to open the image (or stack image in 3D) and then open the module in "plugin/Multifractal soil analysis/2D Gliding Multifractal" for 2D images or "plugin/Multifractal soil analysis/3D Gliding Multifractal" for 3D images. Then a dialogue (Figure 19) will be appear

where the user has to define the range of the multifractal exponents q , giving its minimum, maximum value and one interval.

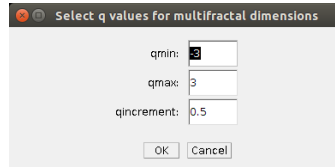


Figure 19: Dialogue about q exponents

The gliding box method accept all size of images. Finally and before show the plots and tables, a dialogue (Figure 20) will be appear with a countdown to estimate the time it would cost to make all the calculations.

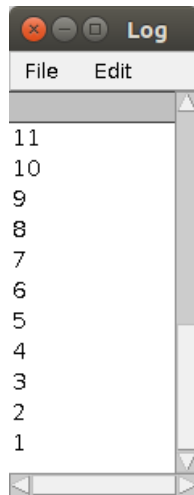


Figure 20: Countdown

Then will appear a dialogue (Figure 21) where the user can choose to analyze the actual image or the inversed one.

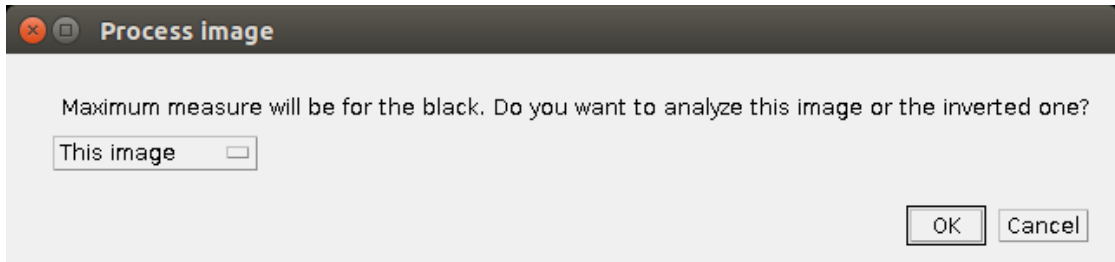


Figure 21: Choose between the actual image or the inverted one

Then the user can select the minimum and maximum size of the boxes (in pixels) that will be used along analysis. In Figure 22 the numbers shows are the limits that can be chosen.

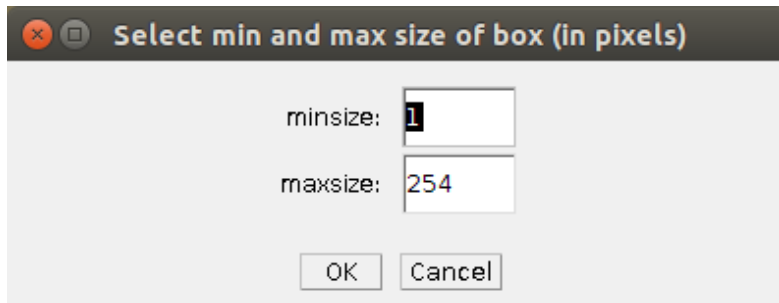


Figure 22: Choose the maximum and minimum size of the boxes for the analysis

3.2 Example 3: Landsat TM imagery

For this example we are going to analyse a Landsat TM imagery (see Figure 23), captured on 7 September, 1985 covering about 350 km^2 in the Michell-Sulphirets mineral district, northwestern BC, Canada [8]. For applying multifractal analysis to this image we are going to select a minimum size of box size of 1 pixel and a maximum size of box equal to the width of the image.



Figure 23: Landsat TM band 5 from 7 September, 1985. Copied directly from a pdf file in [8]

While the program is doing the calculations a windows similar to Figure 20 will show a countdown which give us an idea about how much time it will cost to getting the results. Then the first plot (Figure 24) shows $X(q)$ vs ϵ for each value of q . If the line get saturated or have different slopes along ϵ we can run again the program for choosing more properly the minimum and maximum size of the boxes.

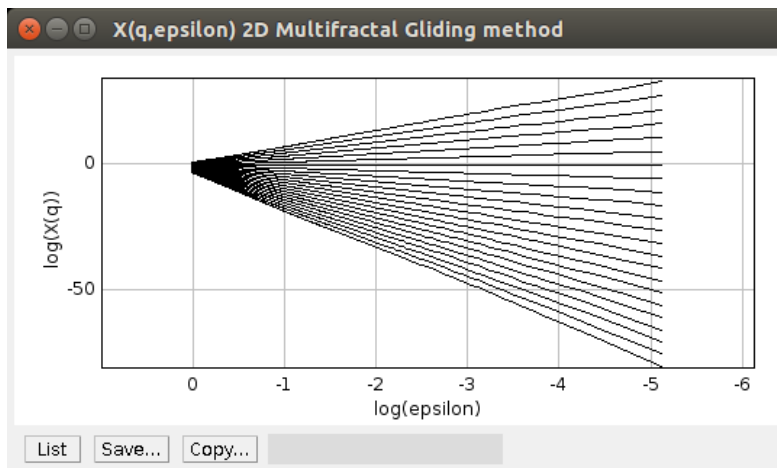


Figure 24: $X(q, \epsilon)$ vs ϵ for each q based on multifractal Gliding Method

Pushing 'List' it shows the numeric values of the plot.

Then, τ is calculated for each q as the slope of $X(q, \epsilon)$ and shown in Figure 25. The numerical values and the errors can be get pushing in the 'list' window. Here we compared them with the ones in [6]. The numerical values are virtually identical.

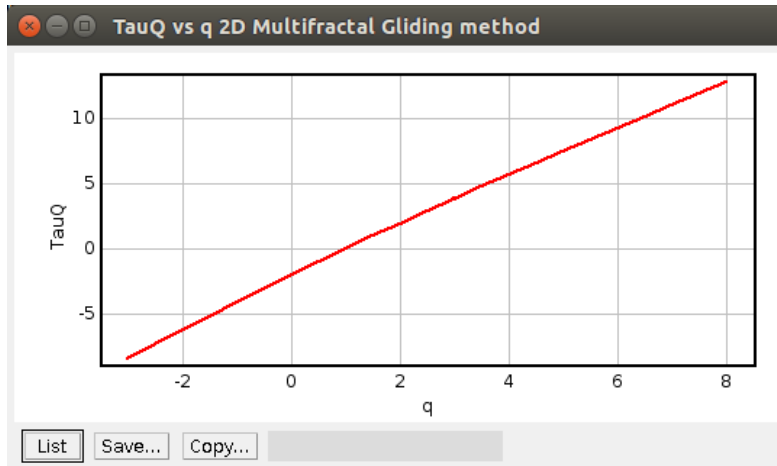


Figure 25: τ vs q . It is also plotting the errors of τ but in this case they are too small for being appreciated.

Pushing 'List' it shows the numeric values of τ for each q and its error.

Dq is easily calculated as $Dq = \frac{\tau}{q-1}$ and shown in Figure 26.

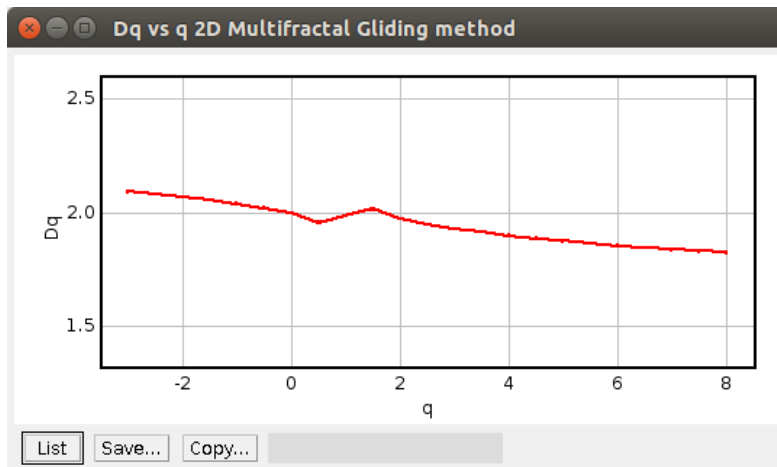


Figure 26: Dq vs q . Errors of Dq very small for being appreciated in the plot.

Pushing 'List' it shows the numeric values of D_q for each q and its error.

For the Gliding Method the calculate of α has been done through numerical derivation of τ . They are estimated by means of the central difference method from $\tau(q)$ and a step $h = 0.01$. Figure 27 shows α vs q .

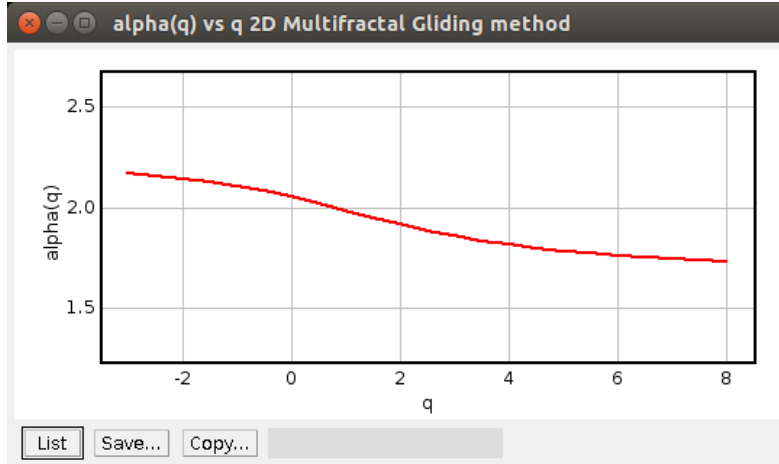


Figure 27: α vs q based on multifractal Gliding Method

Pushing 'List' it shows the numeric values of α for each q and its error.

Finally $f(\alpha)$ is calculated as $f(\alpha) = q\alpha - \tau$ and shown in Figure 28

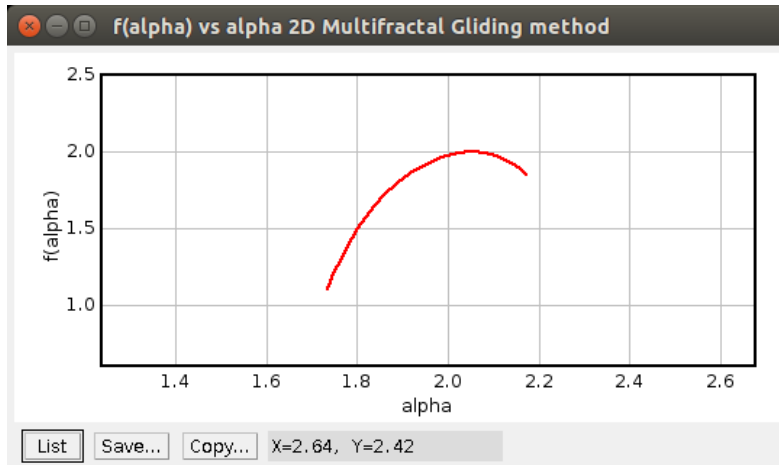


Figure 28: Multifractal spectrum $f(\alpha)$ vs α using Gliding Method

Here the numeric values are not shown in 'List' button. The α and $f(\alpha)$ values with their errors for each q are shown in a table that the program shows.

References

- [1] *ImageJ online manual*.
- [2] Benoit B Mandelbrot. *The fractal geometry of nature*. Macmillan, 1983.
- [3] Ashvin Chhabra and Roderick V Jensen. Direct determination of the $f(\alpha)$ singularity spectrum. *Physical Review Letters*, 62(12):1327–1330, 1989.
- [4] Hse Tzia Teng, Hong-Tat Ewe, and Sin Leng Tan. Multifractal dimension and its geometrical terrain properties for classification of multi-band multi-polarized sar image. *Progress In Electromagnetics Research*, 104:221–237, 2010.
- [5] E Perfect, RW Gentry, MC Sukop, and JE Lawson. Multifractal sierpinski carpets: Theory and application to upscaling effective saturated hydraulic conductivity. *Geoderma*, 134(3):240–252, 2006.
- [6] Qiuming Cheng. The gliding box method for multifractal modeling. *Computers & Geosciences*, 25(9):1073–1079, 1999.
- [7] J Grau, V Méndez, AM Tarquis, MC Díaz, and A Saa. Comparison of gliding box and box-counting methods in soil image analysis. *Geoderma*, 134(3):349–359, 2006.
- [8] A Rencz, J Harris, and SB Ballantyne. Landsat tm imagery for alteration identification. *Current research E*, 1994:277–282, 1994.